

1 **Preservation of Organic Carbon in Dolomitized Cambrian Stromatolites and Implications**  
2 **for Microbial Biosignatures in Diagenetically Replaced Carbonate Rock**

3 ASHLEY E. MURPHY<sup>a\*</sup>, SCOTT T. WIEMAN<sup>b,c,d</sup>, JULIANE GROSS<sup>e</sup>, JENNIFER C. STERN<sup>c</sup>, ANDREW  
4 STEELE<sup>f</sup>, and MIHAELA GLAMOCLIIA<sup>a</sup>

5 <sup>a</sup>*Rutgers University, Department of Earth and Environmental Sciences, 101 Warren St, Smith Hall*  
6 *– Room 135, Newark, NJ, 07102 (\*corresponding author e-mail: ashley.murphy@rutgers.edu)*

7 <sup>b</sup>*Center for Space Sciences and Technology, University of Maryland, Baltimore, MD 21250, USA*

8 <sup>c</sup>*Planetary Environments Laboratory, NASA Goddard Space Flight Center, Greenbelt, MD 20771,*  
9 *USA*

10 <sup>d</sup>*Center for Research and Exploration in Space Science and Technology, NASA Goddard Space*  
11 *Flight Center, Greenbelt, MD 20771, USA*

12 <sup>e</sup>*Department of Earth and Planetary Sciences, Rutgers University, New Brunswick, NJ 08854,*  
13 *USA*

14 <sup>f</sup>*Geophysical Laboratory, Carnegie Institution of Washington, Washington, DC, 20015, USA*

15 **ABSTRACT**

16 Stromatolites have been a major focus in the search for ancient microbial biosignatures, in  
17 particular, stromatolites containing silicified microfossils. Silicification allows for the preservation  
18 of original textures and morphologies, which are important starting criteria in the characterization  
19 of fossils' biogenicity and syngenicity to host rock. The microbial biosignatures of dolomitized  
20 stromatolites have not yet been characterized and correlated with their dolomitizing conditions.  
21 The Cambrian Allentown Formation in New Jersey is an excellent example of dolomitized  
22 stromatolites and thrombolites containing diagenetically modified microbial biosignatures. Based  
23 on XRD, ICP-OES, and EPMA data, the dolomite is ordered, and all three generations of dolomite  
24 are stoichiometric. The outcrop underwent early dolomitization by meteoric diagenesis and burial  
25 diagenesis resulting in multi-generational dolomite formation as follows: (1) The microspar  
26 dolomite formed by early replacement of precursory calcium carbonate minerals, at or very near

27 the surface, where mixing of fresh and marine waters produced finely crystalline dolomite, (2) The  
28 zoned dolomite formed penecontemporaneously with the microspar phase as rhombohedral  
29 crystals by infilling primary pore spaces within the microspar matrix. Cloudy cores observed in  
30 many larger dolomite rhombs indicate recrystallization before the crystals grew outward in  
31 alternating stages, preserved in zoned rims, of Fe-enriched and -depleted fluids, (3) The saddle  
32 dolomite formed during late stage deeper burial with Fe- and Mn-rich fluids and occurs as void-  
33 filling, high-temperature phase. Organic carbon, characterized using confocal Raman microscopy,  
34 is exclusive to first generation microspar dolomite, and the D and G bands' characteristics reveal  
35 similar style thermal alteration as host rock, indicating that the mapped organic carbon is  
36 syngenetic with the Cambrian stromatolites. This study offers a new way to investigate ancient life  
37 signatures preserved in secondary dolostones and may aid biosignature detection in ancient  
38 carbonate rocks on Mars.

39

40 *Keywords:* dolomitization, Cambrian stromatolites, organic carbon, biosignature, meteoric  
41 diagenesis, burial diagenesis

42

## 43 **1. INTRODUCTION**

44 Stromatolites are microbially mediated sedimentary structures that record the oldest forms of  
45 life on Earth (Barghoorn and Tyler, 1965; Grotzinger and Knoll, 1999; Allwood et al., 2006).  
46 These ancient structures have been a significant focus of both geo- and astrobiology because  
47 silicification during early diagenesis provides exceptional preservation of original textures and  
48 organic chemistry, which are the leading indicators in the characterization of biogenicity and  
49 syngeneticity (Knoll et al., 1988; Buick, 1990; Grotzinger and Knoll, 1999; Van Kranendonk et al.,

50 2003; Sugitani et al., 2007; Schopf and Kudryavtsev, 2012; Braiser et al., 2015). Unlike  
51 silicification, dolomitization commonly results in the loss of original microstructural details of  
52 microbial fossils (Schopf, 1999; Bartley et al., 2000), making the characterization of syngenetic  
53 and indigenous biosignatures ambiguous (Grotzinger and Rothman, 1996). As the calcium  
54 carbonate grains solidify to limestone, the developing crystals press the microorganisms between  
55 grain boundaries as they grow, thereby destroying cellular morphology (Schopf, 1999).

56 Although studies of biosignatures in dolomitic stromatolites have been reported, they have  
57 been interpreted as primary dolomite precipitation (Rao et al., 2003; Ayllón-Quevedo et al., 2007;  
58 Sanz-Montero et al., 2008; Calça et al., 2016) within which fossils were preserved exclusively in  
59 silica (Ayllón-Quevedo et al., 2007; Sanz-Montero et al., 2008; Calça et al., 2016) or sulfur-rich  
60 mineral phases (Lindtke et al., 2011). The effects of dolomitization, as a secondary process when  
61 devoid of silicification, on the preservation of microbial biosignatures, have yet to be thoroughly  
62 interpreted. The identification and characterization of indigenous and syngenetic biosignatures  
63 preserved in a host rock that has undergone secondary dolomitization alteration are complicated  
64 due to loss of the original microbial morphologies. Although the original texture is commonly  
65 obliterated by later replacement and recrystallization processes, dolomitization settings vary, and  
66 some of the temperature and pressure parameters associated with it may be conducive to the long-  
67 term preservation of the indigenous organics. The syngeneticity of this type of fossilization in the  
68 geologic record can only be comprehensively examined after the degree of alteration of the host  
69 rock has been appropriately characterized and evaluated against that of the biologic remains.

70 The gap in knowledge of dolomitized microbial biosignature preservation is further  
71 complicated when applied to astrobiology. Carbonate lithologies are a recognized astrobiology  
72 target for Mars exploration, and the primary science goal of the Mars 2020 mission is to determine

73 whether life existed on Mars by seeking signs of extinct life in the rock record (Mustard et al.,  
74 2013). Although the origin of the magnesium carbonates identified at the Martian paleolake Jezero  
75 Crater (~4-3.5 Ga) is still uncertain (Ehlmann et al., 2008; Goudge et al., 2015), the crater may  
76 contain lacustrine carbonate deposits (Horgan et al., 2020) which are habitable environments on  
77 Earth that are capable of biosignature preservation. Therefore, terrestrial analogs of ancient  
78 magnesium carbonates, such as dolostone, will allow for better interpretation of potential  
79 biosignatures in Martian carbonates.

80 In this paper, measurements of whole rock, bulk carbonate, and high-resolution in situ analysis  
81 of each generation of dolomite is used to characterize the dolomitization setting to evaluate the  
82 level of diagenetic alteration that has affected the analyzed stromatolitic outcrop, and the effect  
83 such alteration had on the preservation of indigenous microbial biosignatures within these  
84 Cambrian carbonates.

85

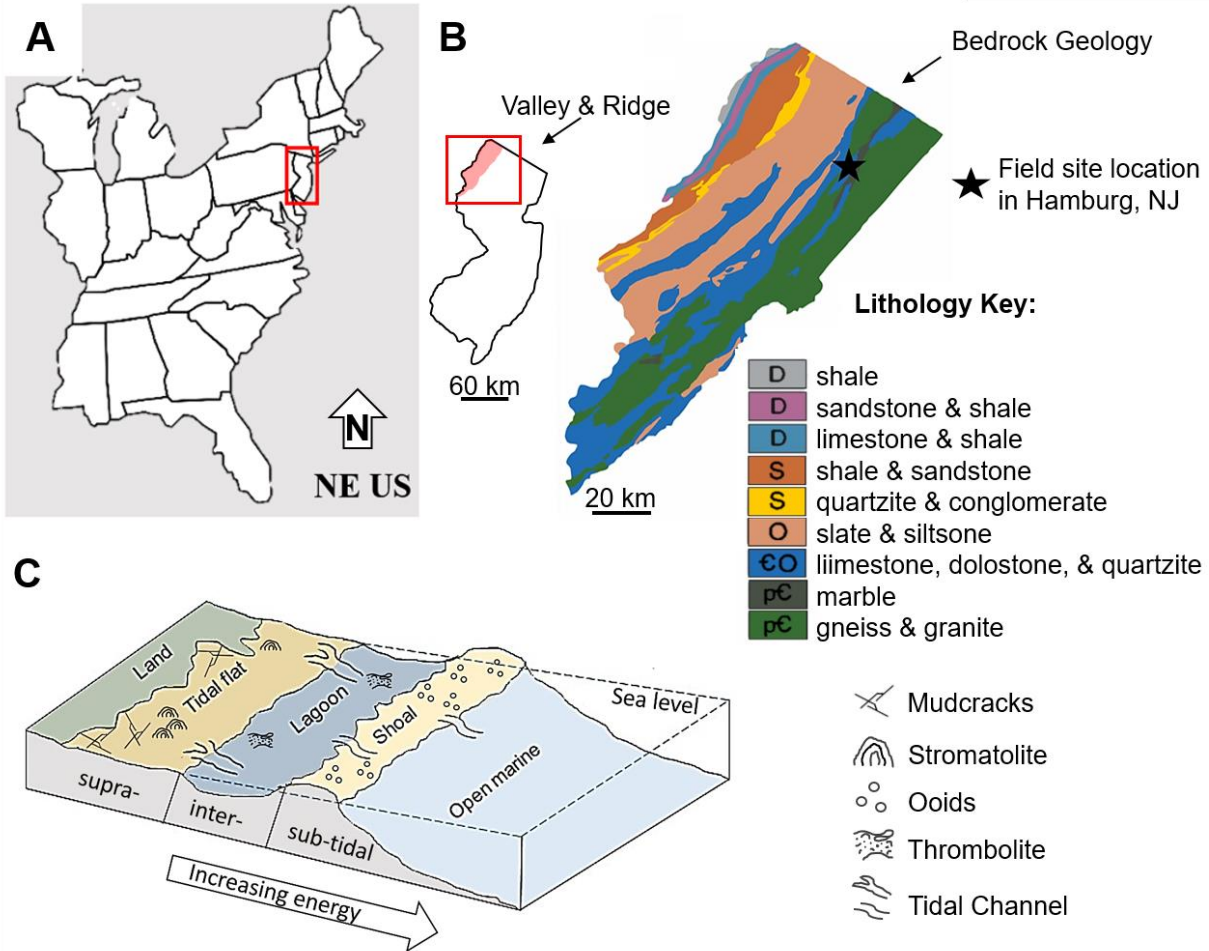
## 86 **2. GEOLOGIC SETTING**

### 87 **2.1. Regional geology and sedimentology**

88 The Late Cambrian (515-500 Ma) Allentown Formation (Weller, 1903; Howell, 1945; Harris  
89 et al., 1995; Dalton et al., 2014), commonly referred to as Allentown Dolomite, is part of the  
90 Kittatinny Supergroup (542-443 Ma) which is a northeast-trending belt (Fig. 1 B) that records the  
91 formation of the eastern Laurentian passive margin, when the deposition of shallow-water  
92 carbonates dominated, and sediments from eroding inland rocks were transported by streams to  
93 the coast and deposited on the shallow shelf (Miller, 1941; Dalton et al., 2014).

94 Paleoreconstruction of the area shows the ancient North American landmass, Laurentia,  
95 positioned below the equator and rotated approximately 90° clockwise from its current orientation.

96 The paleoenvironment has been interpreted as a shallow subtidal to supratidal setting dominated  
 97 by limestone deposition that later dolomitized (Miller, 1941; Stead and Kodama, 1984; Dalton et  
 98 al., 2014). The Taconic orogeny of the Late Ordovician period (~440 Ma) is recorded in the uplift,  
 99 folding, and faulting in the region, which was further deformed by the Alleghanian orogeny during  
 100 the Permian period (~270 Ma) (Miller, 1941; Drake, 1965; Dalton et al., 2014).



101 **Fig. 1.** Geologic map and sampling location. (A) Location of New Jersey (NJ) within the United  
 102 States of America. (B) Location of the studied Allentown Formation outcrop (marked by star) in  
 103 Hamburg, NJ. The Cambrian to Middle Ordovician Kittantiny Supergroup (blue lithology) of  
 104 the Valley and Ridge Physiographic Providence in NJ (red shaded area within red box of inset  
 105 NJ map). Modified from Witte and Monteverde (2012). (C) Reconstruction of paleoenvironment  
 106 based on outcrop observations in this study. Modified from Pratt et al. (1992).  
 107

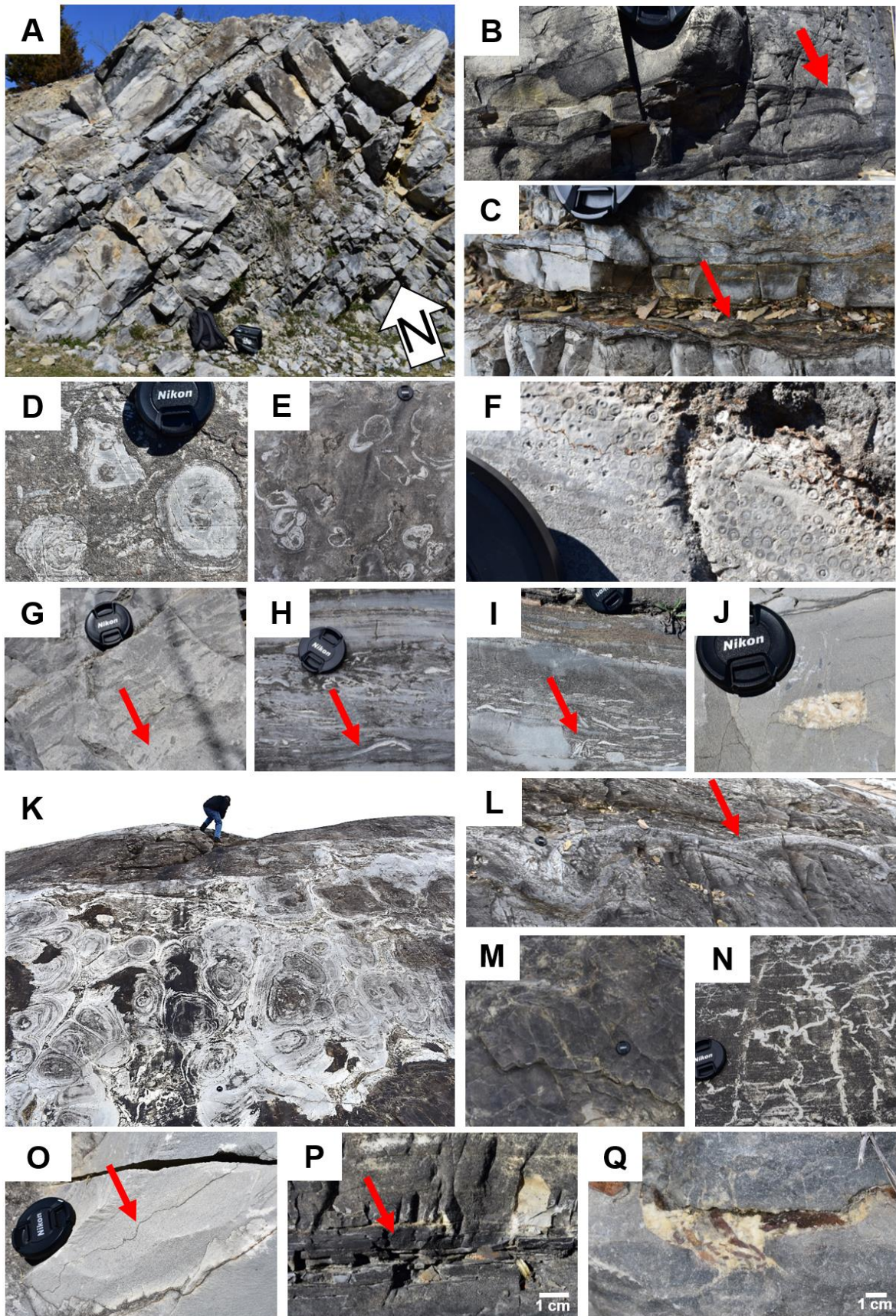
108 Previous geologic mapping of the Allentown formation reveals that the bedding varies (from  
 109 oldest to youngest) as follows: textureless dololutite (<0.0039 mm grain size), dolarenite (0.0625-

110 2 mm), oolitic dolarenite (0.0625-2 mm), dolorudite (>2 mm), cryptozoan dolomite, and  
111 desiccation dolorudite (>2 mm) (Drake Jr., 1965). In areas of large exposure, these beds repeat in  
112 a cyclic manner, where individual cycles range in thickness from ~2 to 10 m, and the entire  
113 formational sequence measures up to 580 m thick (Drake Jr., 1965; Monteverde, D.H., 1992). In  
114 the 1950s, the Allentown was referred to as two members, (from bottom to top) the Limeport and  
115 Allentown members (Drake Jr., 1965). This distinction was made in older literature because the  
116 lower Limeport member contains numerous 'cryptozoan' (hereafter referred to as stromatolites)  
117 of various morphologies, including large domes with convex-shaped laminae, wavy beds, and  
118 small domes of laterally linked lamina (Drake Jr., 1965).

## 119 **2.2. Study area**

120 The study area in Hamburg, New Jersey is 40 m of uplifted dolostone, tilted 44° NW. Exposure  
121 along the southwestern side of the outcrop (Fig. 2 A and Fig. 3 column A) allows for measurements  
122 of bedding thickness that are elsewhere inexact due to glacially polished rock surfaces. Along the  
123 longest transect, the outcrop is 100 m long with extensive vegetation cover that limits correlation  
124 between the northeast and southwest parts of the outcrop (Fig. 3). The transect analyzed in the  
125 middle of the outcropping area (Fig. 3 column B) includes before mentioned stromatolites. The  
126 bottom of the transect is ~13 m of fine-grained, grey dolosiltite intercalated with iron oxidized  
127 dissolution seams that are weathered black in outcrop (Fig. 2 B). The occurrence of thrombolites  
128 is marked by a brown wavy layer of ~1 cm thick laminae (Fig. 2 C). The thrombolites are overlain  
129 by small ( $\leq 5$  cm) round stromatolite heads (Fig. 2 D and E) that continue to occur periodically in  
130 overlying strata for ~20 m. Massive oolitic dolarenite (Fig. 2 F) is situated above the stromatolite  
131 heads for ~11 m. The oolitic grainstone is overlain by ~13 m of dolosiltite with numerous beds of  
132 high energy, storm deposit features such as of rip-up clasts (Fig. 2 G) edgewise conglomerates

133 (Fig. 2 H), and jumbled intraclasts (Fig. 2 I). These beds co-occur with coarse-grained dolomite-  
134 filled vugs ( $\leq 9$  mm) (Fig. 2 J). Large ( $\leq 30$  cm) domal stromatolites are observed at the top of the  
135 formation and surrounded by intraclasts, and collapse breccia (Fig. 2 K). The NE side of the  
136 outcrop reveals the convex up structure of the domes (Fig. 2 L) Mudcracks are situated above the  
137 large domal stromatolites (Fig. 2 M) and syneresis cracks are observed southwest of the  
138 stromatolites (Fig. 2 N). Wavy stylolites parallel to bedding are found throughout the formation  
139 (Fig. 2 O). Chert occurs as black lenses or thin layers ( $\sim 1$  cm) throughout the formation (Fig. 2 P).  
140 This bedding sequence corresponds with a shallowing upward peritidal sequence (Fig. 1 C and see  
141 5.1.).



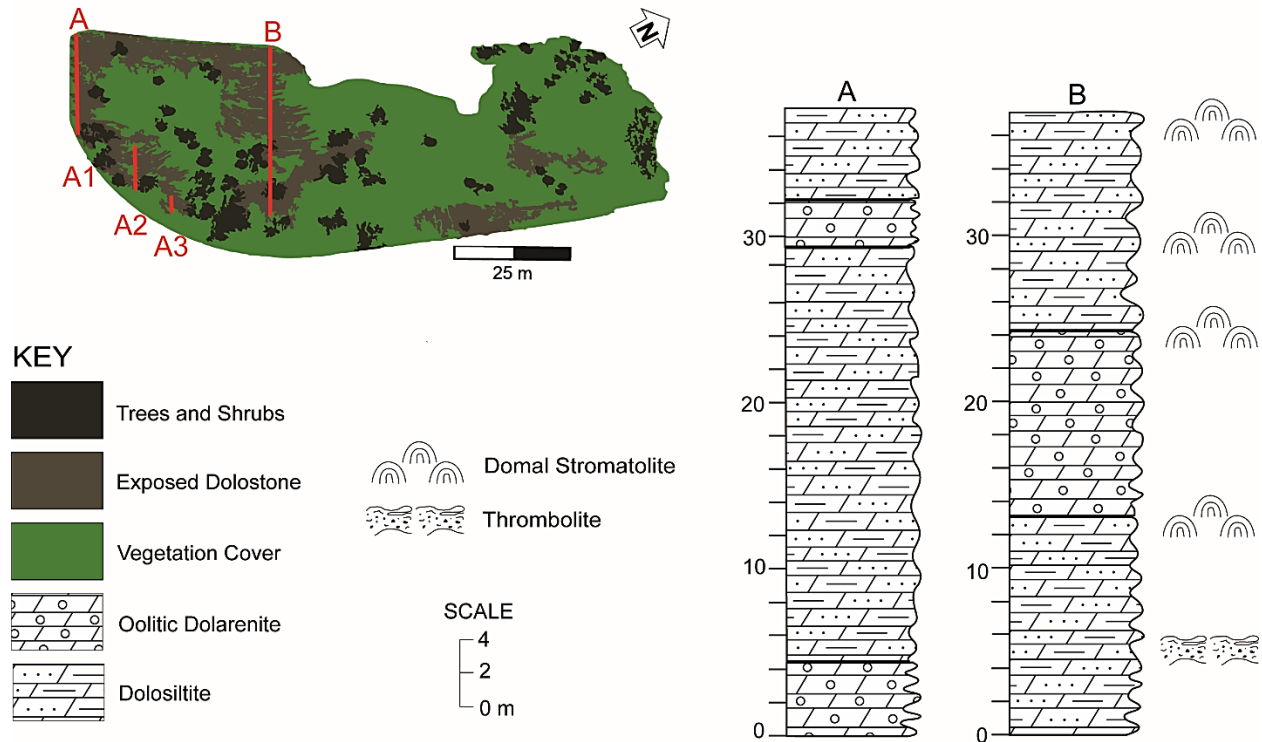


143 **Fig. 2.** (A) Side view of formation with tilted layers dipping 44° NW. (B) Dolosiltite intercalated  
144 with solution seams. (C) Brown crinkled layer (red arrow) marks the top of thrombolites (D)  
145 Small stromatolite heads. (E) Ripped up stromatolite heads. (F) Ooid grainstone. (G) Dark grey  
146 rip-up clasts. (H) Edge-wise conglomerates. (I) Jumbled intraclasts. (J) Large vug filled with  
147 coarse-grained dolomite. (K) Top of formation with glacially smoothed domal stromatolites (L)  
148 convex upward shape of stromatolites from NE side of outcrop. (M) Mudcracks and (N)  
149 syneresis cracks visible from top of formation. (O) Wavy stylolite parallel to bedding. (P) Black  
150 chert lens. (Q) Collapsed stylolite material into coarse-grained dolomite filled vug. Nikon camera  
151 lens (5.5 cm radius) used for scale.  
152

### 153 **3. MATERIALS AND METHODS**

#### 154 **3.1. Sampling strategy**

155 Samples were collected from 2017 to 2020 in Hamburg, NJ. The sampling strategy included  
156 twenty-two different sampling points, from bottom to top of the formation, while targeting obvious  
157 stromatolitic morphologies and significant changes in strata texture or appearance. Table 1 lists  
158 samples from bottommost (A12d) to the topmost bedding layers (A18). All samples were collected  
159 in an organically clean manner to avoid contamination by using gloves to handle samples that were  
160 wrapped in sterile aluminum foil and placed in canvas bags. Subsampling was performed in the  
161 laboratory using a diamond blade saw and DI water to cut away outer rock layers from the interior  
162 areas that were later used for analyses.



163  
 164 **Fig. 3.** Stratigraphic columns from sampling area. Column A is exact bedding thickness  
 165 measured along A1, A2 and A3 (marked red on outcrop figure). Column B is estimated thickness  
 166 along glacially smoothed bedding measured along B (marked red). Outcrop figure modified from  
 167 aerial Google Earth imagery. Note the lateral differences in both columns and lack of microbial  
 168 structures observed at Column A.  
 169

### 170 3.2. Petrographic and mineralogical analyses

171 Petrographic analyses of 14 representative layers were used to describe the stromatolites and  
 172 associated dolostone. The petrographic study involved plane polarized and cross polarized light  
 173 inspection of thin sections for textural and mineral identification, as well as to target regions of  
 174 interest for further spectroscopy.

175 The detection of minor mineral phases was performed by Scanning Electron Microscopy with  
 176 Energy Dispersive X-ray Spectroscopy (SEM/EDS) using a Hitachi S-4800 operating at 15 to 20  
 177 kV and 12 to 15 uA, equipped with an Apollo X EDAX at Rutgers University in the Department  
 178 of Chemistry.

179 Qualitative elemental X-ray mapping and cathodoluminescence (CL) mapping was performed  
180 on 6 thin sectioned samples with an accelerating voltage of 15 kV, a beam current of 14 nA, a  
181 beam diameter of 1 micron, with a 1  $\mu\text{m}$  step size per pixel and 30 ms dwell time. Equipment used  
182 was a JOEL Superprobe JXA-8200 at Rutgers University in the Department for Earth and  
183 Planetary Sciences.

184 Powder X-ray diffraction (XRD) of whole rock samples was used to determine dominant  
185 mineral assemblages in 21 samples. The equipment used was a Bruker D8 at Rutgers University  
186 in the Department of Earth and Environmental Sciences. Operational settings were 40 kV, 25 mA,  
187 and Cu-K $\alpha$  radiation. Quantitative analysis of stoichiometry was determined by the  $2\Theta$  value of  
188 the  $d_{104}$  peak in order to calculate the d-spacing using Bragg's Law (Bragg and Bragg, 1913). The  
189 degree of cation ordering was determined by the intensity ratio of the  $d_{015}$  and  $d_{110}$  peak (Graf and  
190 Goldsmith, 1956).

### 191 **3.3. Geochemical analyses**

192 The  $\delta^{13}\text{C}_{\text{dolo}}$  and  $\delta^{18}\text{O}_{\text{dolo}}$  of 16 bulk and 7 micro-drilled samples were determined for further  
193 analyses of the origin of dolomite. The bulk samples were prepared and analyzed in triplicate. The  
194 7 micro-drilled samples were sampled from thin-section billets using a Medenbach© microdrill at  
195 Rutgers University in the Department of Earth and Planetary Sciences in order to isolate microspar  
196 and saddle dolomite generations for comparison to the bulk rock, and to target the minimum and  
197 maximum temperatures of formation. The micro-drilled samples were analyzed in, at minimum,  
198 two replicates.

199 Isotope Ratio Mass Spectrometry (IRMS) was used to determine the carbonate diagenetic  
200 setting using a GasBench II System coupled to a Delta V Plus IRMS at NASA Goddard Space  
201 Flight Center in the Planetary Environments Laboratory.  $\text{CO}_2$  was evolved from each sample at

202 60°C using 85% H<sub>3</sub>PO<sub>4</sub>. Samples were acidified in 6N HCl for approximately 48-96 hours and  
203 analyzed for organic carbon abundance, nitrogen abundance, and  $\delta^{13}\text{C}_{\text{org}}$  using an Elemental  
204 Analyzer coupled to a Delta V Plus IRMS at NASA Goddard Space Flight Center in the Planetary  
205 Environments Laboratory.

206 Electronprobe Microanalyses (EPMA) were carried out using the JOEL Superprobe JXA-8200  
207 at Rutgers University in the Department for Earth and Planetary Sciences. Quantitative spot  
208 analyses to isolate each generation of dolomite was performed on 6 samples using an accelerating  
209 voltage of 15 kV, a beam current of 15 nA, and a beam diameter of 5 microns.

210 Chemical analyses of 16 samples using Inductively Coupled Plasma - Optical Emission  
211 Spectroscopy (ICP-OES) was carried out at Rutgers University in the Department of Earth and  
212 Environmental Sciences to access the bulk carbonate concentration of major (ppm) and trace (ppb)  
213 cations using an Agilent 5510. The digestion method used was based on the EPA procedure 3052.  
214 All samples were analyzed in triplicate, and average values are reported.

### 215 **3.4. Confocal Raman microscopy and thermometry**

216 Confocal Raman Microscopy and Spectroscopy was used for spot analyses and mapping of 14  
217 thin sections and 8 unprocessed rock samples, to determine the organic carbon spatial distribution,  
218 associations with minerals, and to analyze the D and G bands ( $\sim 1350$  and  $1600\text{ cm}^{-1}$ , respectively)  
219 characteristic Raman signal for the organic matter. Five thin sections were chosen for the final  
220 high-resolution analysis, these representative layers ranged across the top, middle, and bottom  
221 areas of the outcrop and include all lithological textures observed at the outcrop. This work was  
222 performed with a WITec alpha300 equipped with a frequency-doubled Nd:YAG (532 nm)  
223 excitation laser. Operational settings were as follows: a 1 mV average laser intensity (range from  
224 1-3 mV) to minimize laser-induced heating and to avoid structural modification of the samples,

225 and a depth of 1-5  $\mu\text{m}$  below the surface to was used to avoid surface contamination. Mapped areas  
226 were visually inspected by transmitted and reflected light microscopy for holes and cracks in the  
227 samples that may contain polishing grit, epoxy, or other contaminants related to sample handling  
228 that may interfere with the D and G band spectra. Samples that could not be unambiguously  
229 identified as unaffected by this type of contamination or were too friable for thin sectioning were  
230 not included in the final Raman data sets.

231 D and G bands were analyzed in two ways for data quality assessment, using 1) WITec  
232 Project FIVE+ software cluster analysis and, 2) WITec Project FIVE+ software Gaussian fitted  
233 background subtraction. The cluster method identifies variations in D and G band phases within  
234 a map, averages it, and displays a distribution map. Ten clusters of spectral variations were  
235 calculated from each map, and one to three were chosen from each mapped area after quality  
236 evaluations (signal-to-noise ratio, surface contamination, and interference bands from hematite  
237 were avoided after being inspected both visually and spectrally). The Gaussian fit method uses a  
238 Savitzky-Golay filter to smooth the graph before applying background subtraction using a  
239 Gaussian fit for both the G and D bands. The average D and G band peak centers are displayed  
240 on a distribution map where one to three spectral points, representative of different spectral  
241 trends, were hand selected. Maps were inspected for visual and spectral interferences as listed  
242 above in the cluster analysis method.

243 All spectra were normalized to facilitate comparison. Band intensities were normalized by  
244 taking the height of each band and dividing it by the most intense G band in the spectrum. Data  
245 collected from both methods were exported as ASCII files into Excel and used to calculate the  
246 Raman parameters of the D/G intensity ratio, peak area, and the Raman shifted peak position. A  
247 two-tailed, two-sample *T*-test ( $p=0.05$ ) was applied to D and G spectral data to determine if

248 variations within the bands were statistically different. The peak table exported from the WITec  
249 software was used to report the full width at half maximum (FWHM) for both D and G bands.

250 Thermometry was calculated using the D1 band geothermometer from Kouketsu et al. (2014):

$$251 \quad T(^{\circ}\text{C}) = -2.15 * (\text{FWHM-D1}) + 478 (\pm 30^{\circ}\text{C})$$

252 This geothermometer was chosen due to the consistency of FWHM with temperature (Kouketsu  
253 et al., 2014) and the spectral characteristics of the Allentown's D and G peaks which do not  
254 exhibit an obvious D2 peak within the G peak.

255

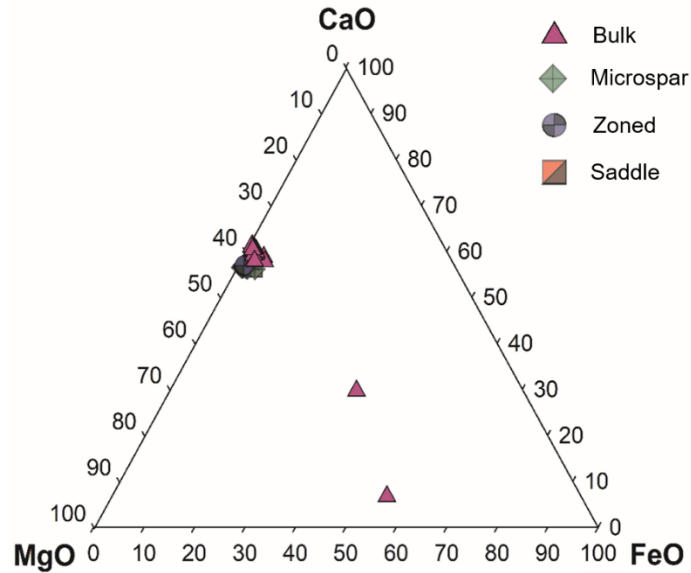
## 256 **4. RESULTS**

### 257 **4.1. Allentown petrology and mineralogy**

#### 258 *4.1.1. Bulk mineralogy*

259 Based on Powder X-Ray Diffraction (XRD) (Fig. S1 in supplementary material) the lithology  
260 of the Allentown Formation is predominantly dolomitic with few  $\pm 1$  to 40 cm thick, greyish-black  
261 chert lenses, and  $\pm 1$  cm brown colored feldspathic carbonate layers (samples A15, A15b, and A6,  
262 respectively).

263



264 **Fig. 4.** Ternary diagram comparing stoichiometry from ICP-OES bulk carbonate MgO, CaO,  
 265 and FeO concentrations (pink triangles) to EPMA measured MgO, CaO, and FeO concentrations  
 266 for separate dolomite generations (see legend). The two outliers of bulk carbonate composition  
 267 are the feldspathic (A6) and cherty dolomite samples (A15). All dolomitic samples cluster in the  
 268 dolomite range of the diagram, near 40 to 45% MgO and 55 to 60% CaO composition.  
 269

270 The feldspathic (orthoclase and microcline) carbonate layers occur as thin wavy layers or disk-  
 271 shapes and are commonly observed along fractured bedding surfaces or at the top of microbial  
 272 macrostructures. The average d-spacing of the dolomite  $d_{104}$  peak is 2.89 Å (n=21), while the range  
 273 in degree of cation order calculated by the  $d_{015}/d_{110}$  intensity ratio is 0.36 - 0.99 (Table 1). Cherty  
 274 and feldspathic carbonate samples did not exhibit d peaks of (015) or (110) in XRD, and therefore  
 275 these samples were not included in the stoichiometry and cation ordering averages.

Sample ID	Sample Description	Degree of Cation Order ( $d_{015}/d_{110}$ )	Stoichiometry				
			P-XRD $d_{104}$ -spacing	ICP-OES Mg/Ca (ppm)	EPMA (avg. elemental wt %)		
					Micritic	Zoned	Saddle
A18	dolarenite mudcracks	0.654	2.890	-	-	-	-
A17	feldspathic dolarenite tidal channel deposit	0.604	2.888	-	-	-	-
A16	dolosiltite domal stromatolite	0.599	2.886	0.566	0.621	0.620	0.602
A15a	chert lens	n/a	n/a	4.800	-	-	-
A14	oolitic dolosiltite	0.659	2.893	0.530	0.621	n/a	0.586
A13	oolitic dolosiltite	0.619	2.893	0.534	-	-	-
A12a	oolitic dolarenite	0.848	2.893	0.530	0.628	0.629	n/a
A11	dolarenite	0.989	2.884	0.537	0.628	0.628	n/a
A10	oolitic dolarenite	0.640	2.893	0.533	0.622	n/a	n/a
A9	oolitic dolosiltite	0.491	2.893	0.529	-	-	-
A8	dolosiltite	0.375	2.893	0.532	-	-	-
A7	oolitic dolosiltite	0.900	2.893	0.527	0.619	0.630	n/a
A6	feldspathic dolosiltite disk	n/a	2.888	0.939	-	-	-
A5	oolitic dolosiltite thrombolite	0.596	2.885	0.525	-	-	-
A4	dolosiltite	0.737	2.894	0.529	-	-	-
A3	dolosiltite with microstylolites	0.683	2.893	0.525	0.618	0.625	n/a
A2	dolosiltite with solution seams	0.363	2.894	0.551	-	-	-
A1	dolosiltite with solution seams	-	-	0.543	-	-	-
A15b	dolomitic chert lens	n/a	2.854	-	-	-	-
A12b	oolitic dolarenite	0.656	2.889	-	-	-	-
A12c	oolitic dolarenite	0.772	2.891	-	-	-	-
A12d	oolitic dolarenite	0.788	2.890	-	-	-	-

dolosiltite = silt sized grains (5  $\mu$ m - 63  $\mu$ m)

n/a denotes no data from analysis

dolarenite = sand sized grains (63  $\mu$ m - 2 mm)

- denotes the sample was not analyzed

276  
277  
278  
279  
280  
281

**Table 1.** Stoichiometry and cation order within samples listed from bottommost to topmost sampled strata, A12d to A18, respectively. Cation order ranges from 0.36 – 0.99 and indicates the Allentown dolomite is relatively well to well ordered. Values from XRD d-spacing, ICP-OES and EPMA Mg/Ca ratios all indicate the Allentown dolomite is stoichiometric.

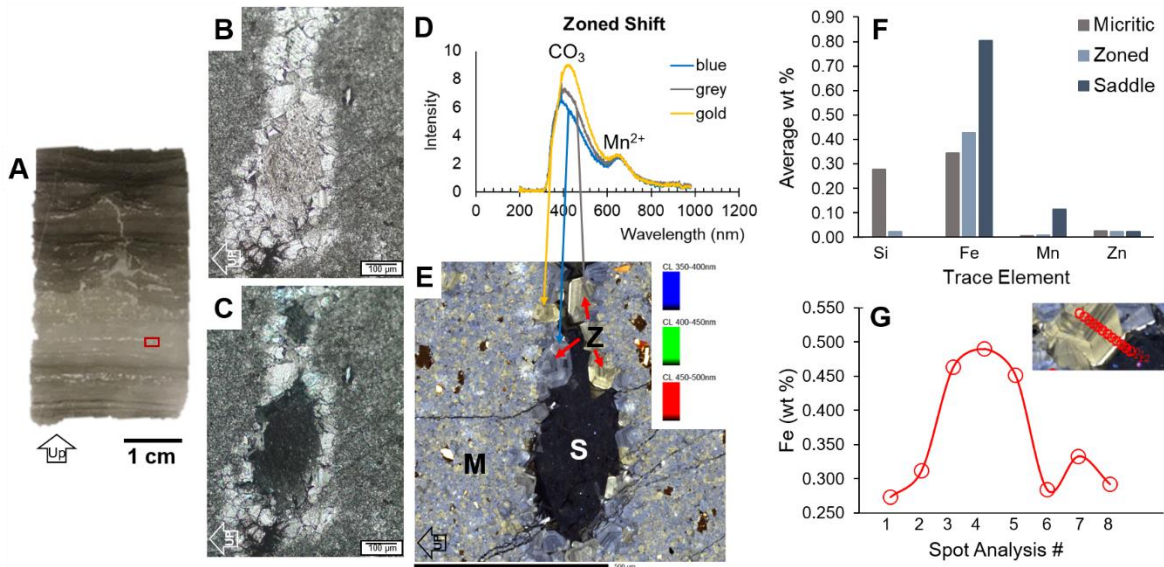
## 282 4.2. Microtextures and mineralogy

### 283 4.2.1. Multi-generational dolomite characterization

284 Composite Red-Green-Blue (RGB) cathodoluminescence maps with R = 450-500 nm, Green  
285 = 400-450 nm, and Blue = 350-400 nm reveals three distinct generations of dolomite in all  
286 analyzed samples. Dolomite generations vary in crystal size, shape, and intercrystalline  
287 boundaries. Based on the nomenclature from Sibley and Gregg (1987), the three generations of  
288 dolomite are classified and characterized from oldest to youngest as microspar, zoned, and saddle.  
289 The microspar dolomite is nonplanar, has closely packed anhedral crystals with irregular,  
290 intercrystalline grain boundaries. The crystals average 20 microns and range 5-40 microns in size.

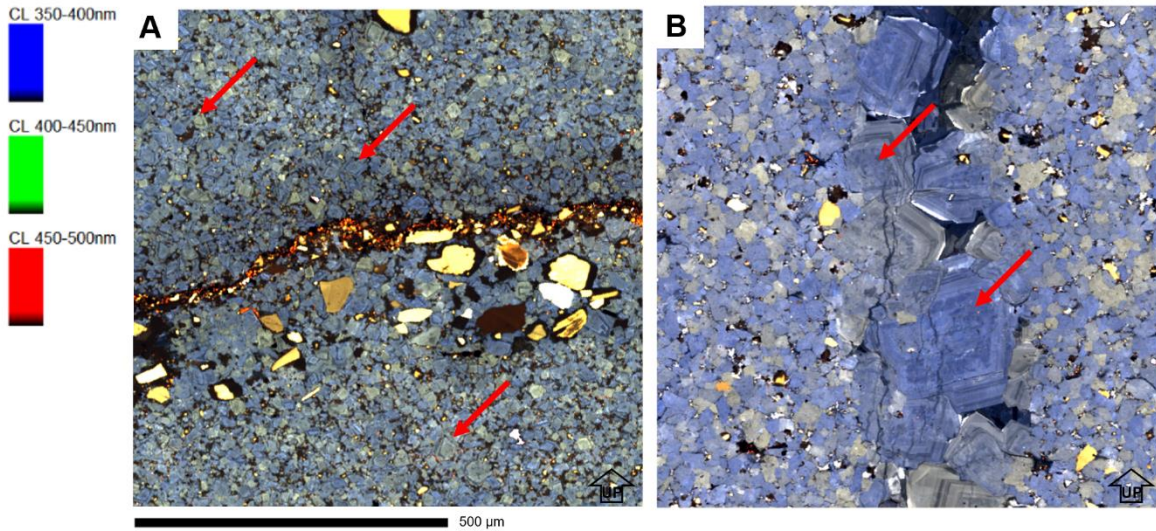


291 Zoned dolomite is planar, subhedral to anhedral medium grained (10-100 microns) with straight  
 292 compromised boundaries. The crystals are concentrically zoned in CL and characteristically pore  
 293 lining or void-filling (Fig. 5 E and Fig. 6). Saddle dolomite is nonplanar, medium (10-100 microns)  
 294 to coarse grained (>100 microns) saddle-shaped, void-filling, and exhibits undulatory extinction  
 295 in cross polarized light (Fig. 7 A3 and A4). The three observed CL colors, by increasing  
 296 wavelength are blue, grey, and gold, and are found throughout the zoned and microspar dolomite  
 297 generations; the saddle dolomite exhibits a dull bluish color in CL. Throughout each generation of  
 298 dolomite, two CL spectral peaks are present at 389 nm and 650 nm.



299 **Fig. 5** CL and EPMA results. (A) Thin section of domal stromatolite. Red box indicates mapped  
 300 area in (E). (B) Plane polarized light photomicrograph of fenestral pore from sample (A). (C)  
 301 Cross polarized light photomicrograph of (B). (D) Characteristic spectra of luminescence colors  
 302 showing a peak shift at CO<sub>3</sub>. (E) CL map showing three generations of dolomite: microspar (M),  
 303 zoned (Z), and saddle (S). (F) EPMA spot analyses across each generation of dolomite showing  
 304 the dolomitizing fluid compositional changes. (G) EPMA spot analysis across zoned dolomite  
 305 reveals dark zonation bands are Fe-enriched.

306



307 **Fig. 6** (A) CL map of microstylolite from dolosiltite sample A3 showing zoned rhombohedral  
 308 dolomite in pores of the microspar dolomite matrix (red arrows). Numerous feldspars (larger  
 309 yellow-brown grains) can be seen near the solution seam. (B) CL map of vertical microfracture  
 310 in dolarenite sample A11 showing zoned dolomite that lines and fills the microfracture. The  
 311 rhombohedral dolomite cores appear cloudy (red arrows), indicating recrystallization.  
 312

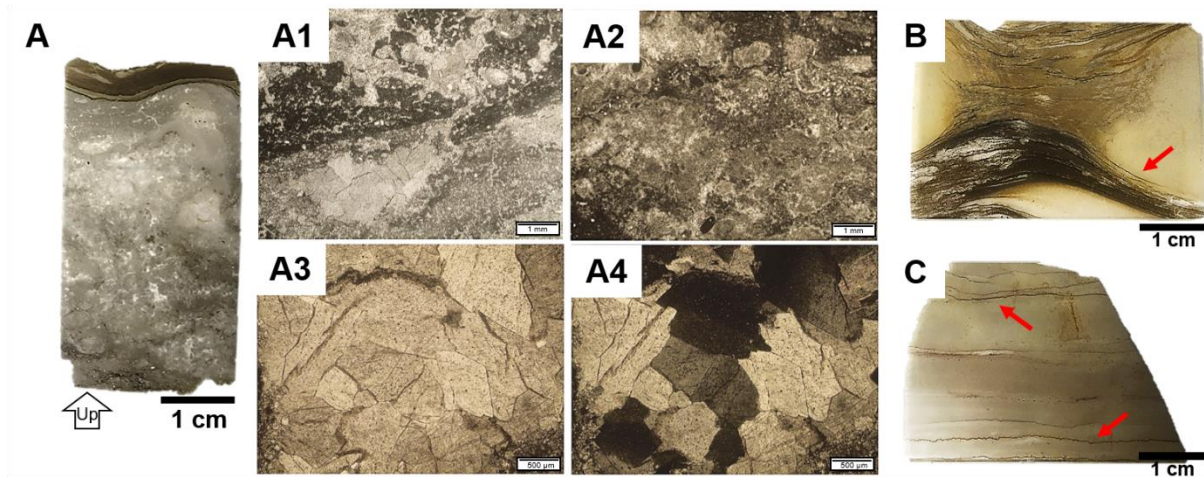
313 *4.2.2. Porosity types and dissolution features*

314 Open porosity is absent in the studied samples, but occluded pore types of primary and  
 315 secondary origins were observed. Primary fenestral porosity ( $\leq 1$  mm in size) is ubiquitous in  
 316 stromatolite samples and infilled with zoned and saddle dolomite (Fig. 8 B1, B3, and B4).  
 317 Secondary microfractures occur in two stages. The first stage includes vertical microfractures ( $< 1$   
 318 mm wide), infilled with zoned and saddle dolomite, that are present in limited layers of microspar  
 319 dolomite, and crosscut horizontal laminae and fenestrae in the domal stromatolite (Fig. 8 A3). The  
 320 second stage includes randomly oriented microfractures ( $< 1$  mm wide) that are present in the  
 321 oolitic dolosiltite sample A14 and are only infilled with saddle dolomite. Vugs are large secondary  
 322 pores that are at least two times greater in size than the microspar matrix, the vugs are in average  
 323 2 mm to 9 mm in size and are infilled with zoned and saddle dolomite (Fig. 2 J). Vugs occur  
 324 predominately in storm layers with rip-up clasts and are absent from the lowermost lagoonal facies.

325 Dissolution structures of numerous solution seams occur on fresh surfaces as brownish,  
326 irregular streaks but appear black on weathered surfaces, and are abundant in the lowermost  
327 outcrop layers of lagoonal facies of the lower outcrop layers of finely crystalline, microspar  
328 dolomite samples (Fig. 7 B). The seams are Fe oxidized stained but composed of dolomitic  
329 material, likely as a result of dolomite dissolution. Microstylolites that parallel laminae occur  
330 throughout sample A3 (Fig. 7 C). Stylolites are either dolomitic in composition or, when found  
331 along fractured bedding planes, are infilled with quartz, feldspars, and iron oxides.

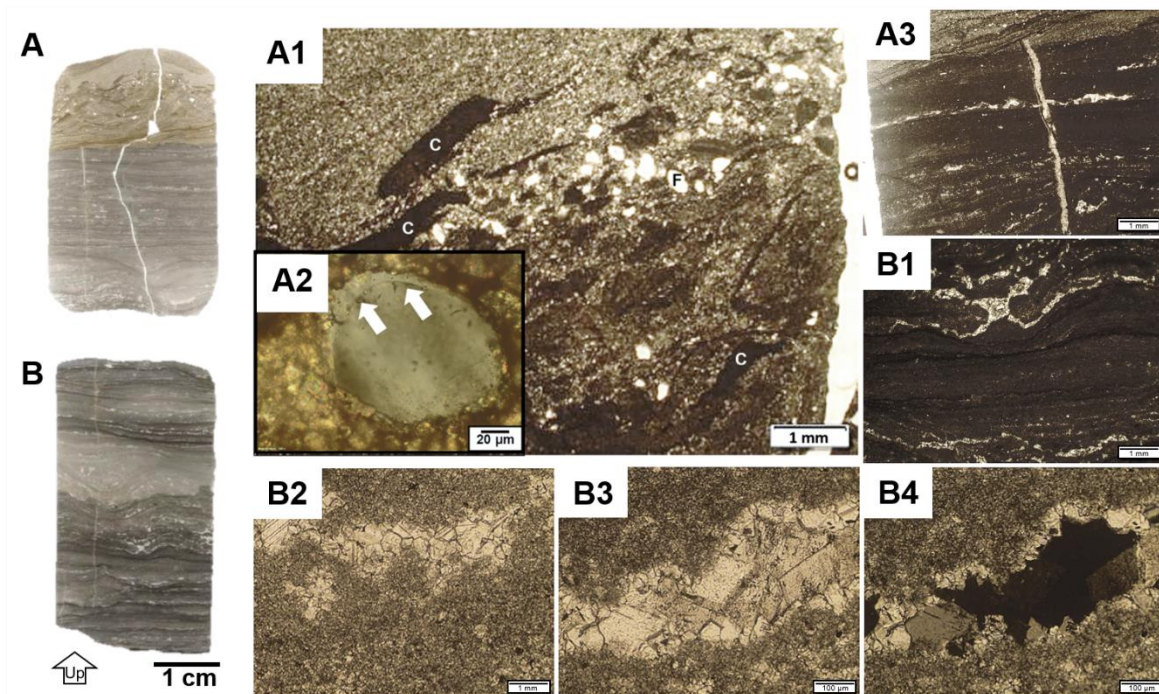
#### 332 4.2.3. *Thrombolites*

333 The thrombolites exhibit clotted, irregular microtextures (Fig. 7 A1 and A2). Rounded  
334 microcline and orthoclase, and sub-rounded quartz occur throughout the sample, with sparse  
335 amounts of peloids and ghost grains. SEM/EDS reveals minor mineral components of Fe-oxides  
336 and pyrite grains. The detected metal oxide morphologies range from euhedral to highly deformed  
337 in shape, and the pyrite has round to sub-round edges (Fig. S2 in supplementary material).



338 **Fig. 7** Subtidal lagoonal facies microtextures. (A) Thin section of thrombolite sample. (A1)  
339 Plane polarized light (ppl) 2.5x magnification of clotted structure and large saddle dolomite-  
340 filled vug. (A2) Ppl 2.5x magnification of clotted thrombolite structure. (A3) Ppl 5x  
341 magnification of large saddle dolomite filled vug, indicative of burial dolomitization. (A4) Cross  
342 polarized light (xpl) of (A3) shows sweeping extinction characteristic of saddle dolomite. (B)  
343 Thin section of dolosiltite sample (A1) with wispy solution seams (red arrow). (C) Thin section  
344 of dolosiltite sample (A3) with microstylolites (red arrows).

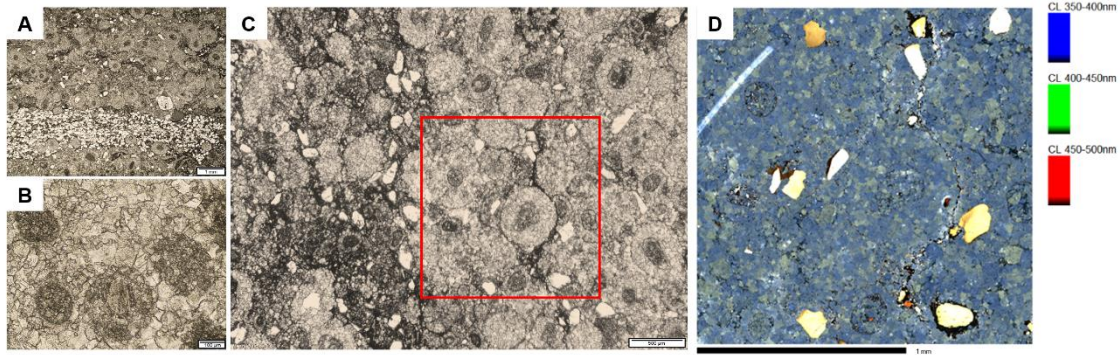
345



346 **Fig. 8** Tidal flat stromatolitic facies microtextures. Thin sections of the top (A) and bottom (B) of  
 347 a large domal stromatolite sample with corresponding photomicrographs: (A1) Plane polarized  
 348 light (ppl) 2.5x magnification of rip-up clasts (marked C) and feldspars (marked F) within  
 349 topmost portion of dome indicate a tidal channel deposit. (A2) Confocal Raman micrograph of  
 350 an orthoclase overgrowth rim (white arrows) indicate thermal alteration. (A3) Ppl 2.5x  
 351 magnification showing preservation of primary fenestral porosity that is crosscut by secondary  
 352 microfracture porosity, evidence for early, near-surface dolomitization. (B1) Ppl 2.5x  
 353 magnification showing very fine laminae of finely crystalline dolomite, common to tidal flat  
 354 stromatolites. Fenestra (light colored areas in image) is filled with zoned and saddle dolomite.  
 355 (B2) Ppl 2.5x magnification of microspar dolomite and coarser-grained zoned dolomite-filled  
 356 fenestrae. (B3) Ppl 25x magnification of zoned and saddle dolomite-filled fenestrae surrounded  
 357 by microspar. (B4) Cross polarized light (xpl) of (B3).  
 358

#### 359 4.2.4. Ooids

360 The oolitic dolomite layers exhibit a dissolution-fill microstructural type of dolomite (Scholle  
 361 and Ulmer-Scholle, 2003) with little or no original texture (radial, tangential, or otherwise)  
 362 visible except for a dark-colored ooid outline and relics of concentric layers near the nucleus of  
 363 the ooid (Fig. 9). Ooids vary in size from ~0.25 to 1 mm in diameter.



364 **Fig. 9** Oolitic grainstone microtextures observed in thin sections. (A) Plane polarized light (ppl)  
365 photomicrograph 2.5x magnification of ooids (sample A10) with a finer-grained siliceous layer  
366 near the bottom of the image (white area). (B) Ppl photomicrograph 25x magnification of ooids  
367 from (A) showing dolomite replacement. (C) Ppl photomicrograph 5x magnification of CL  
368 mapped area (red box) in (D). (D) CL map showing characteristic violet luminescence. Bright  
369 white and yellow grains are feldspars.  
370

#### 371 4.2.5. *Stromatolites*

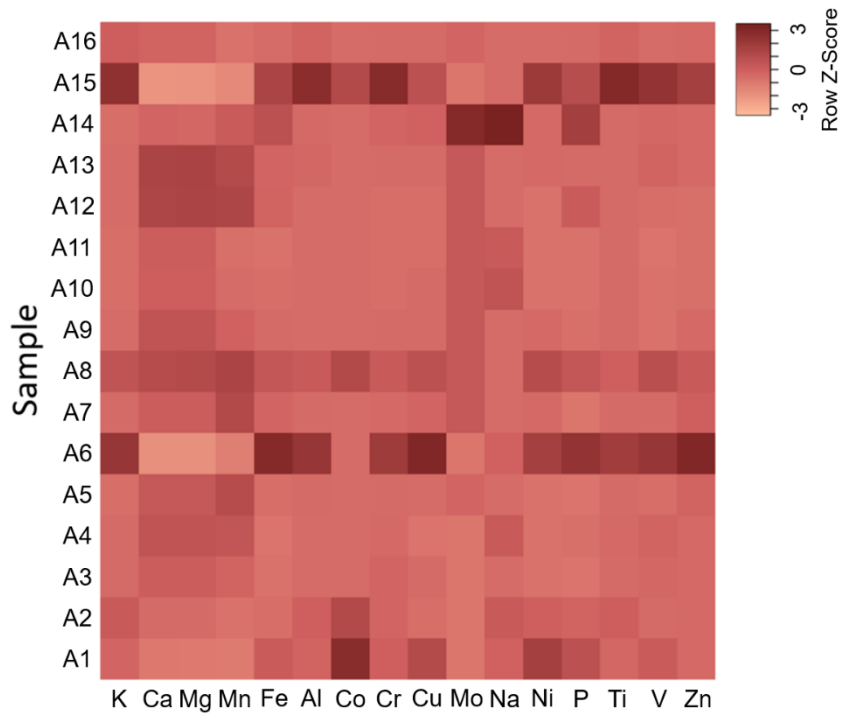
372 The microtexture of domal stromatolites is thinly layered convex-shaped layers of alternating  
373 dark (<1 mm thick) and light grey ( $\leq 1$  cm thick) laminae (Fig. 8 A and B) and some very thin (<1  
374 mm) layers appear black (Fig. 8 B). EDS showed no differences in composition between dark and  
375 light grey bands of laminae, however, the black laminae is enriched in felsic material. Primary  
376 fenestral porosity ( $\leq 1$  mm thick) in the domal stromatolite is parallel to laminae and infilled with  
377 zoned and saddle dolomite. Very fine-grained, rounded intraclast rip-ups are situated on the  
378 topmost layer (Fig. 8 A1), which also contains large (<0.5 mm in diameter), rounded feldspars of  
379 microcline and orthoclase, and sub-rounded quartz grains. The orthoclase minerals exhibit  
380 overgrowth rims (Fig. 8 A2). The SEM/EDS reveals Ti-oxides, Fe-oxides, and apatite as minor  
381 mineral components (Fig. S2 in supplementary data).

382

### 383 4.3. Geochemistry

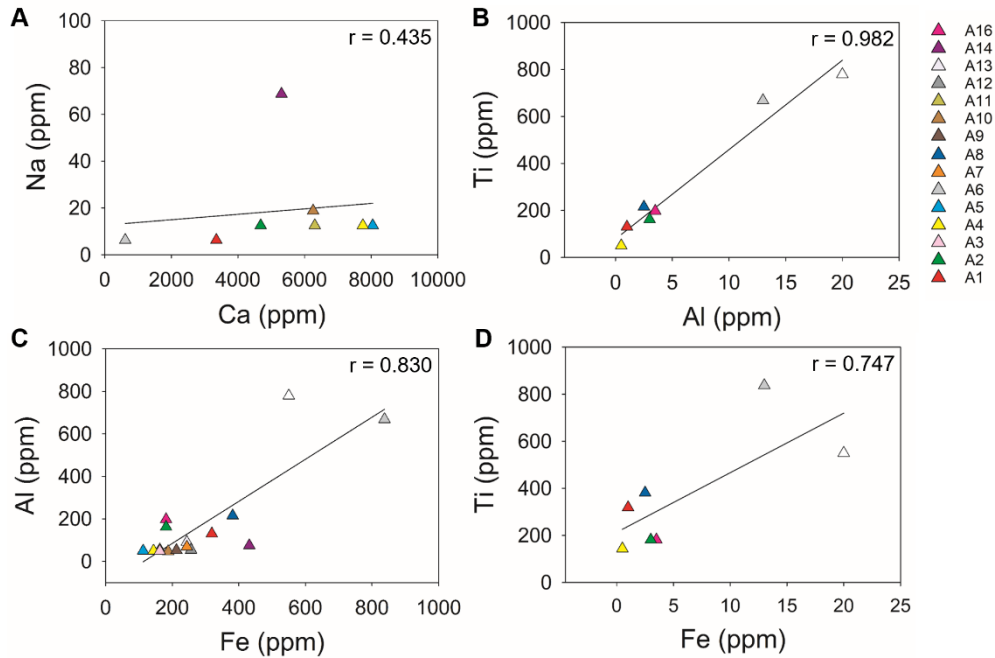
#### 384 4.3.1. *Bulk carbonate elemental analysis*

385 Measurements by ICP-OES reveal that there is no major difference in bulk dolomite  
386 geochemistry across the samples among the Allentown layers except for the chert and feldspathic  
387 carbonate lithological outliers described in section 4.1 (A15 and A6). These layers exhibit  
388 relatively higher concentrations of Al, Cr, Fe, K, P, Ti, V, and Zn (Fig. 10 and Table S1 in  
389 supplementary material). ICP-OES reveals cherty layers contain 5x more titanium (Ti) than is  
390 detected in the other analyzed samples (Table S1 in supplementary material). Raman spectra  
391 show TiO<sub>2</sub> is predominantly anatase with minor amounts of rutile. Transition metals of Sr, Mo,  
392 Cu, Co, Ni, W, Cr, V are found in low concentrations (0.05 to 1.55 ppm) or are below detection  
393 limits (<DL). Na is detected in half of the samples (18.75 ppm average). The Mg/Ca  
394 stoichiometry values, average 0.53 ppm for all samples, excluding the values obtained from  
395 layers A15 and A6 (Fig. 4).



396

397 **Fig. 10** ICP-OES bulk carbonate geochemical data. Composition heatmap of samples A1 to A16  
 398 (bottommost to topmost bedding). Row Z-score legend is the number of standard deviations from  
 399 the mean (Z-score of 0 = the mean value). Cherty and feldspathic samples, A15 and A6,  
 400 respectively, are enriched in various trace elements, as compared to dolomitic strata that does not  
 401 differ much in bulk comparison.



402 **Fig. 11** ICP-OES results showing elemental relationships. (A) Weak correlation between Ca and  
 403 Na. (B) Strong correlation between Al and Ti. (C) Strong correlation between Fe and Al. (D)  
 404 Strong correlation between Fe and Ti. Bi-plots for (B) through (D) indicate that Al, Fe, and Ti  
 405 are from the same lithogenous source(s).  
 406

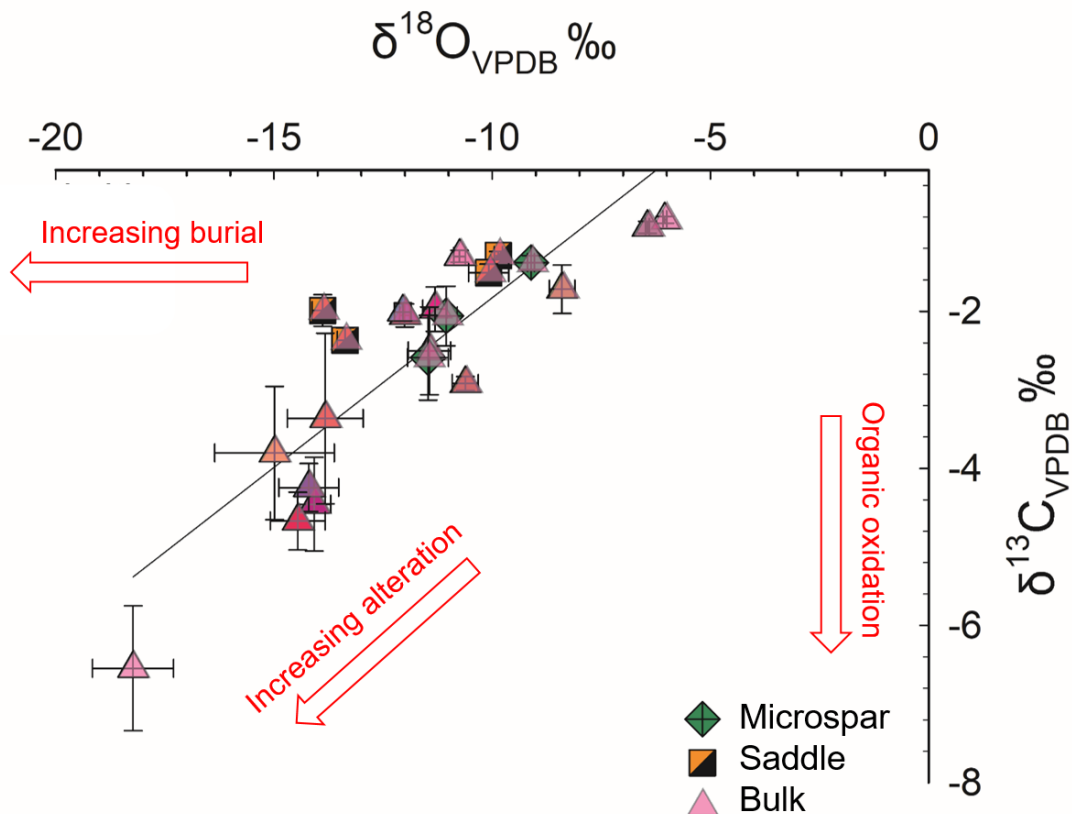
#### 407 4.3.2. Multi-generational dolomite high-resolution elemental analysis

408 Each generation of dolomite was targeted for microanalyses by electronprobe after  
 409 identification with CL. All three generations of dolomite contain Zn and Mn, and the microspar  
 410 and zoned dolomite generations have Si (Fig. 5 F). The zoned dolomite exhibits dark banding  
 411 associated with Fe concentrations of 0.4 wt % or higher (Fig. 5 G). A compositional trend is  
 412 observed in the microspar and zoned dolomite generations by a covarying increase in Si with a  
 413 decrease in Ca and Mg. A decrease in Si abundance and an increase in Fe and Mn abundance is  
 414 observed across each generation of dolomite. No Sr is detected in any generation. The cation

415 ordering of Mg/Ca ratios averaged, 0.63 (n=116 spots analyzed), 0.63 (n=130), and 0.59 (n=131)  
416 wt % for microspar, zoned, and saddle dolomite generations, respectively (Table 1 and Table S2  
417 in supplementary material).

#### 418 4.3.3. Carbonate $\delta^{18}\text{O}$ and $\delta^{13}\text{C}$ composition

419 Isotope analysis reveals relatively low values of  $\delta^{18}\text{O}_{\text{dolo}}$  (‰ VPDB) and  $\delta^{13}\text{C}_{\text{dolo}}$  (‰ VPDB).  
420 Oxygen isotopes ( $\delta^{18}\text{O}_{\text{dolo}}$ ) range from -18.23‰ to -6.05‰ referenced to VPDB with an average  
421 standard deviation of 0.39‰ (Fig. 12 and Table S3 in supplementary material). Inorganic carbon  
422 isotopes ( $\delta^{13}\text{C}_{\text{dolo}}$ ) range from -6.54‰ to -0.84‰ referenced to VPDB with an average standard  
423 deviation of 0.33‰.



424 **Fig. 12** The  $\delta^{13}\text{C}_{\text{dolo}}$  and  $\delta^{18}\text{O}_{\text{dolo}}$  compositions measured from bulk and micro-drilled  
425 microspar and saddle dolomite generations overlap. Alteration trends are marked by red arrows.  
426 Modified from Allan and Wiggins (1993). The positive covariance in isotopes ( $r=0.85$ ) indicates  
427 alteration from mixed meteoric and marine fluids, and the low isotopic values trend is indicative  
428 of thermal alteration from burial dolomitization.

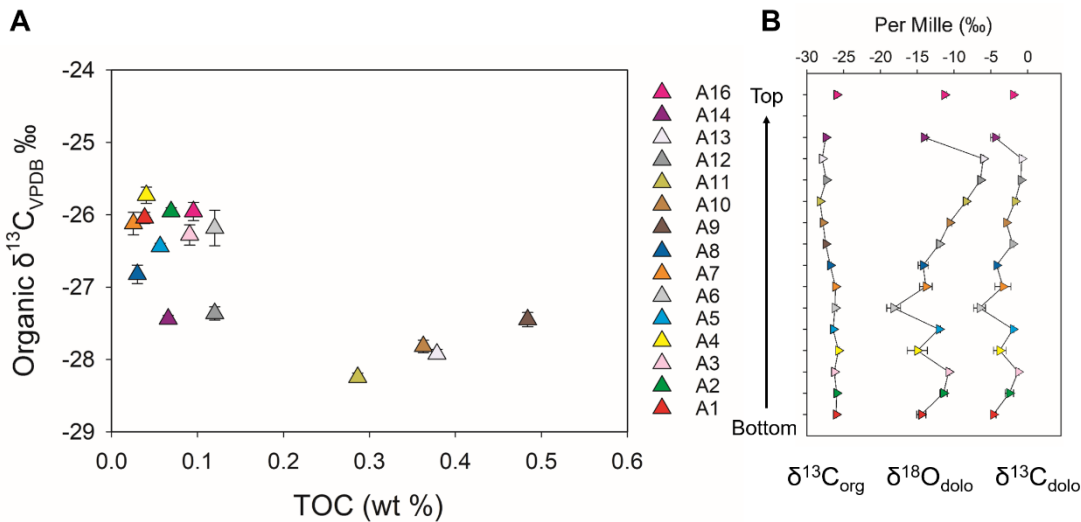


429

430 *4.3.4. Total organic carbon and organic  $\delta^{13}C$  composition*

431 Elemental analysis shows that nitrogen abundance is below detection limits, and organic  
 432 carbon abundance is  $0.16 \pm 0.45$  weight percent with an average standard deviation of 0.002.  
 433 Values of  $\delta^{13}C_{org}$  for organic compounds range from  $-28.25\text{‰}$  to  $-25.73\text{‰}$  referenced to VPDB  
 434 with an average standard deviation of 0.102 (Fig. 13 and Table S3 in supplementary material).

435



436 **Fig. 13** Diagenetic alteration in isotopic trends and TOC. (A) Bi-plot of organic carbon  
 437 abundances (weight percent) and organic carbon isotopic compositions indicating the effect of  
 438 post-depositional alteration. (B) The  $\delta^{13}C_{org}$ ,  $\delta^{18}O_{dolo}$ , and  $\delta^{13}C_{dolo}$  isotopic trends across the  
 439 outcrop reveal coupled  $\delta^{18}O_{dolo}$  and  $\delta^{13}C_{dolo}$  values, but  $\delta^{18}O_{dolo}$  and  $\delta^{13}C_{dolo}$  are decoupled with  
 440  $\delta^{13}C_{org}$  isotopes, indicating post-depositional alteration of  $\delta^{13}C_{dolo}$  values.  
 441

442 **4.4. Confocal Raman microscopy and thermometry**

443 Raman mapping of thin sections reveals that organic carbon, identified by D and G spectral  
 444 bands, is exclusively associated with the microspar dolomite and commonly situated at or near  
 445 grain boundaries. The D and G peaks show slight variations among peak intensity, peak area, and  
 446 peak position (Fig. 14 and Tables S4a and S4b in supplementary material). D and G peak shifts  
 447 within spectral maps are observed in samples A5 and A16, respectively (Fig. 15 B and Fig. S3 in

448 supplementary material). *T*-test results reveal a statistical difference ( $p < 0.05$ ) in some D and G  
449 band positions and FWHM spectral values between stromatolite, thrombolite, and non-microbial  
450 macrostructure samples, as well as in the peak shifts observed in the stromatolite and thrombolite  
451 samples (Fig. S4 in supplementary material). Comparison of the cluster analysis and the Gaussian  
452 fitted data show that the results from the two methods are in good agreement with each other, but  
453 there is a broader range and relative standard deviation in data from the Gaussian fit method (Table  
454 2). This variance in the Gaussian fitted spectra compared to the spectra from the cluster analysis  
455 may be due to more noise in the final spectrum of the background-subtracted Gaussian fitted peaks  
456 related to the difference in number of points selected by hand versus selected by computer in the  
457 cluster process. Cluster analysis shows D/G peak intensity ratios average  $1.00 \pm 0.05$ ; D-FWHM  
458 averages  $68 \pm 34$ ; and D-position averages  $1334 \pm 12$ . Gaussian fit analysis shows D/G peak  
459 intensity ratios average  $1.02 \pm 0.75$ ; D-FWHM averages  $47 \pm 57$ ; and D-position averages  $1335 \pm$   
460 26. All peak parameter results from the cluster and Gaussian fit methods are presented in  
461 supplementary material (Tables S4a and S4b), but the D-band parameters and their related  
462 thermometry will be the focus of this study's results and discussion.

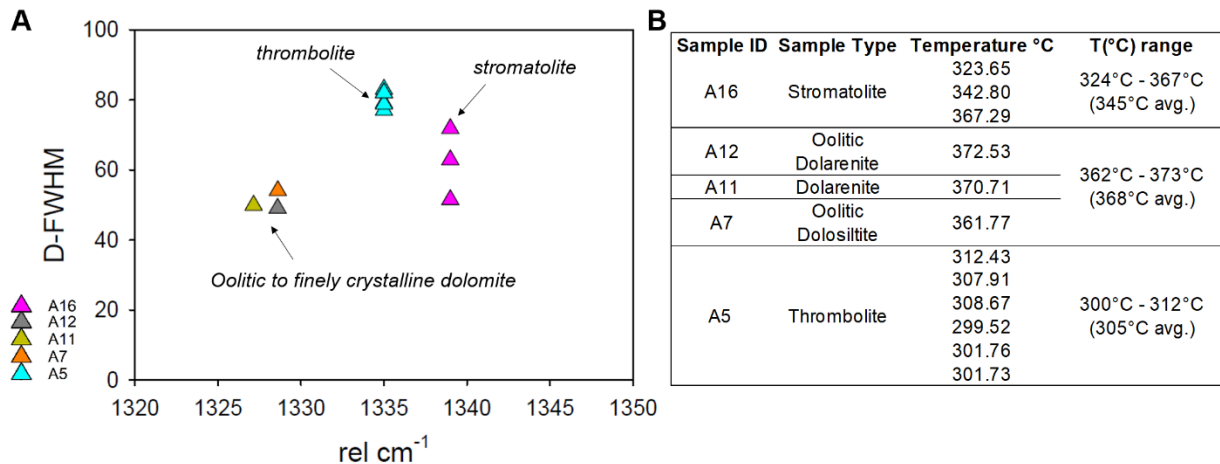
463       Temperatures derived from Raman geothermometry averages  $331^{\circ}\text{C} \pm 73$  and D band  
464 variations show distinct grouping within samples in both peak position ( $\text{rel cm}^{-1}$ ) and FWHM (Fig.  
465 14). The sample grouping correlates to different temperature ranges: highest temperatures  $368^{\circ}\text{C}$   
466  $\pm 11$  in non-microbial samples; moderate temperatures  $345^{\circ}\text{C} \pm 43$  in stromatolite samples; low  
467 temperatures  $305^{\circ}\text{C} \pm 12$  in thrombolite samples (Fig. 14 B). Additionally, the thrombolite and  
468 stromatolite samples A5 and A16 exhibit peak shifts in D and G bands, respectively. These peak  
469 variations, spatially overlapping one another and occurring within the same mapped areas, suggest  
470 different degrees of crystallinity within the organic matter.

471

	<b>Cluster</b>				
	$I_D/I_G$	G-FWHM	G position	D-FWHM	D position
Average	1.00	45.01	1600.54	68.42	1334.28
SD	0.01	3.48	5.29	13.91	4.11
Relative SD	1.40	7.74	0.33	20.33	0.31
Min	0.96	36.43	1594.66	49.06	1327.14
Max	1.02	50.33	1609.00	83.02	1339.00
Range	0.05	13.90	14.34	33.96	11.86
	<b>Gaussian fit</b>				
	$I_D/I_G$	G-FWHM	G position	D-FWHM	D position
Average	1.02	44.21	1599.34	47.29	1335.40
SD	0.18	7.91	5.69	16.54	7.92
Relative SD	17.59	17.90	0.36	34.98	0.59
Min	0.70	25.17	1591.26	19.38	1321.59
Max	1.45	52.83	1608.52	75.88	1347.17
Range	0.75	27.66	17.26	56.50	25.58

472

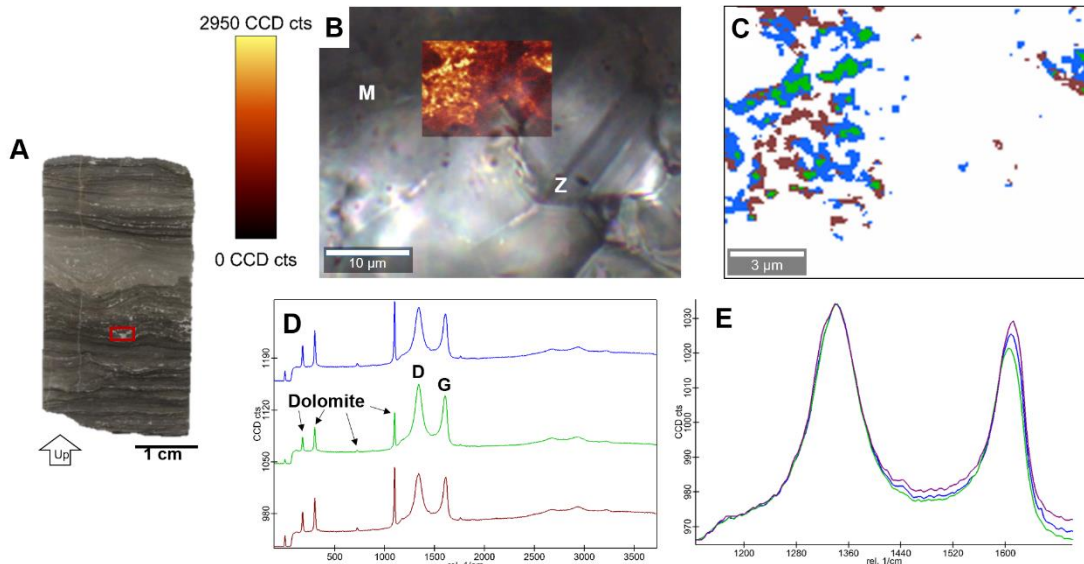
473 **Table 2.** Average D and G band values obtained from the cluster and Gaussian fit methods  
 474 showing comparable values among both peak processing methods used.  
 475



476

477 **Fig. 14.** Raman D band characteristics from cluster method. (A) Samples group together by  
 478 general type. (B) Table of derived temperatures showing temperature variations based on  
 479 grouping in (A).  
 480

481



482 **Fig. 15.** Raman cluster method example. (A) Thin section of domal stromatolite (A16). Red box  
 483 marks area mapped in (B). (B) Transmitted light micrograph of domal sample with overlay of  
 484 Raman mapped D and G bands area. Bright yellow spots within the Raman map indicate spatial  
 485 distribution of D and G bands before the cluster analysis. D and G bands are associated only with  
 486 the microspar generation of dolomite (marked M) but not the zoned crystals (marked Z). (C)  
 487 Raman map after cluster analyses showing differences in D and G bands averages and their  
 488 spatial distribution. (D) corresponding spectra to cluster map (C) with dolomite and carbon peaks  
 489 marked for reference. (E) overlay of D and G bands showing slight peak shift of G band which  
 490 may indicate different levels of crystallinity.  
 491

492 **5. DISCUSSION**

493 The Allentown Formation consists entirely of dolomite, but the sedimentological evidence  
 494 indicates a calcium carbonate precursor mineralogy in a shallowing upward peritidal sequence  
 495 from a transitional marginal-marine setting (Wilson, 1975; Flügel, 2004). Characterization of the  
 496 dolomitization setting, including fluid composition and temperature of formation, is fundamentally  
 497 important when considering syngenicity of fossils within the host rock because the fossils should  
 498 had experienced the same agents of alteration as the host rock. The following sections characterize  
 499 the depositional environment and dolomitization based on outcrop observations, petrological,

500 geochemical, and paleothermometry data, and in what measure the diagenetic history of the  
501 dolostone had affected the alteration of the organic carbon identified within the formation.

### 502 **5.1. Sedimentary facies and paleoenvironment**

503 Exposed stratigraphy displays a shallowing upward, or regressional, sequence where subtidal  
504 high energy ooid shoals transition to intertidal low energy lagoonal waters that progress to a  
505 supratidal mudcracked tidal flat (Fig. 1 C). The massive dolomitized oolitic grainstone beds are  
506 likely from ooid shoals that cut off marine waters and allowed for the development of lower energy  
507 lagoonal waters, which resulted in finer, silt-sized grained beds that overlay the grainstone. The  
508 lagoonal deposits are overlain by finely laminated domal stromatolites that co-occur with extensive  
509 near-shore, subaerial exposure evidence including mudcracks, collapse breccia, and tidal channel  
510 deposits. A near shore, shallow water setting is also indicated by high energy storm evidence  
511 throughout various beds recorded in edgewise conglomerate rip-up clasts, jumbled intraclasts, and  
512 torn laminae in small stromatolite domes (Fig. 2 E). Some layers of lagoonal dolosiltite contain  
513 sparse ooids, referred to as oolitic dolosiltite (Table 1), which are likely the result of wash-over  
514 deposition from ooid shoals during higher tides or storm events.

515 At the top of the outcrop, on the southwest side and adjacent to the large domal stromatolites,  
516 are extensive syneresis cracks (Fig. 2 N). Syneresis cracks form subaqueously (Plummer and  
517 Gostin, 1981), indicating that water levels may have been deeper on this side of the formation.  
518 Further lateral bedding changes are observed in microbial morphologies that are found towards the  
519 northeast side of the outcrop, but not visible from the southwest side of the outcrop. Vegetation  
520 cover limits correlations between lateral bedding differences, and therefore two stratigraphic  
521 columns were made, one for the southwest side of the outcrop (Fig. 3 column A) where bedding  
522 thickness is exactly measured, and one for the northeast side, where bedding thickness is

523 approximated due to glacially polished surfaces (Fig. 3 column B). Column B depicts where the  
524 majority of the samples were collected and includes the various localities of microbial structures.

### 525 *5.1.1. Microtexture and mineralogy*

526 Petrographic microscopy of thin sections supports outcrop observational data. Microtextural  
527 tidal flat paleoenvironmental evidence is apparent in fine-grained dolomite crystals, finely layered  
528 stromatolitic laminae, and channel deposits with rip-up clasts and detrital feldspars and quartz  
529 (Scholle and Ulmer-Scholle, 2003). Similar light and dark grey layering in stromatolite structure  
530 have been reported as organic-poor to organic-rich layers (Grotzinger and Knoll, 1999; Bartley et  
531 al., 2000). Additionally, previous Allentown studies (Buie, 1932; Miller, 1941) have attributed the  
532 color alternation to differing amounts of organic matter and magnesium within the layers, stating  
533 that beds with high Mg weather to a lighter color while beds with lower Mg and more organic  
534 content undergo less change in color during weathering. These inferences cannot be confirmed  
535 here because EDS did not show a difference in Mg content within layers, and Raman mapping  
536 does not show a concentration of organic carbon content in the darker layers, instead data shows  
537 that these layers are rich in felsic material which is likely detrital residue of quartz and feldspars.  
538 The thin dark layers (<1 mm thick) of stromatolitic laminae may have formed during the periods  
539 of minor marine flooding when only the most minute particles were carried across the microbial  
540 mats (Wilson, 1975). Scattered siliceous fine grains are found along some stromatolitic laminae,  
541 and this feature is recorded in regression carbonate evaporitic cycles (Wilson, 1975). Although the  
542 lack of gypsum and anhydrite minerals in this outcrop does not support an evaporitic sabkha  
543 setting, the prolonged subaerial exposure may allow for freshwater flushing to removed evaporitic  
544 minerals and lower Sr and Na trace elements (Land, 1980). Freshwater evidence is supported by

545 ooid microstructures, where coarse dolomite replaced the original calcium carbonate, which is  
546 consistent with freshwater dolomitization (Fig. 9).

#### 547 *5.1.2. Geochemical relationships with deposition and dolomitization*

548 Geochemical evidence of freshwater input is revealed in bi-plots from ICP-OES data (Fig. 11).  
549 Calcium related to original limestone lithology shows a negative correlation with detrital mineral  
550 contributing elements of Fe, Al, Ti, and Na, related to feldspars, which indicate these are indeed  
551 terrigenous materials in the sampled dolostones (Ganai et al., 2018). The acid digestion, although  
552 targeted for carbonate minerals to determine ion substitution in the crystal lattice, may have  
553 partially dissolved oxide and silicate minerals (Voelz et al., 2019), or released fluvial derived  
554 cations that were adsorbed onto the carbonate mineral surface (Swart, 2015). Additionally, the  
555 ratios of Al/Ti ( $r=0.98$   $n=7$ ), Fe/Al ( $r=0.83$ ,  $n=16$ ), and Fe/Ti ( $r=0.75$ ,  $n=7$ ) exhibit positive  
556 correlations indicating a single lithogenous source (Fig. 11 B through D), likely from the  
557 weathering products of inland rocks as previously interpreted (Witte and Monteverde, 2012;  
558 Dalton et al., 2014).

559 Additionally, petrological and SEM micrographs of rounded pyrite and feldspars support a  
560 detrital origin. These minerals make up minor constituents in the whole rock and are most abundant  
561 in the chert and feldspathic carbonate layers. The pyrite is sub- to well-rounded, which is contrary  
562 to a previous study on a Pennsylvanian outcrop that reported cubic pyrite and interpreted this as  
563 an authigenic mineral (Miller, 1941). The distorted Fe- and Ti-oxides observed in this study (Fig.  
564 S2 in supplementary material) were likely altered before deposition and therefore are not indicative  
565 of strain or stress applied to the study area.

566 The relative abundance of major and trace elements in dolomite, including the Mg/Ca ratio,  
567 Fe, Mn, Zn, Sr, Na, and Si concentrations, can reveal the dolomitizing fluid's origin and the

568 formation setting (Morrow, 1982; Tucker and Wright, 1990; Gasparri et al., 2006; Zhang et al.,  
569 2009; Guido et al., 2018). During carbonate diagenesis, concentrations of Sr and Na decrease and  
570 Fe, Mn increase (Wright and Tucker, 1990; Allan and Wiggins, 1993; Warren, 2000). The presence  
571 of Sr and Na is considered a signature of original seawater (Land, 1980; Allan and Wiggins, 1993)  
572 and dolomite formed in the presence of oxidizing surface waters, while Fe and Mn are signatures  
573 of reducing pore water in burial settings (Wright and Tucker, 1990). Traces of original precursory  
574 limestone from the Allentown formation have not been recorded (Dalton et al., 2014), but  
575 assuming the original limestone was deposited in Cambrian marine settings (Miller, 1941; Stead  
576 and Kodoma, 1984; Dalton et al., 2014), any detectable Sr and Na would indicate diagenetic  
577 alteration was relatively low and the dolomitization occurred in the presence of marine waters. No  
578 detectable Sr was found in any of the bulk carbonate samples or multi-generational dolomite spot  
579 analysis; therefore, any original seawater signature associated with Sr, if present, is below  
580 instrument detection limits. Although Na was detected in half (n=8) of the bulk carbonate samples  
581 analyzed from 68.75 ppm and 6.25 ppm, Na shows no correlation to Ca (Fig. 11 A) and is likely  
582 not related to the original seawater but could be from the alteration of Na bearing minerals, such  
583 as clays (Land, 1980; Kirmaci and Akdag, 2005; Li et al., 2015) that could have been adsorbed  
584 onto the carbonate mineral surface (Hu et al., 2005). The Allentown dolostone likely lost its Sr and  
585 Na trace element composition when it dolomitized in the presence of freshwater (Land, 1980;  
586 Allan and Wiggins, 1993). Trace element geochemistry is further discussed in sections 5.2.1.1.  
587 through 5.2.1.3.

## 588 **5.2. Dolomitization**

589 Based on its formation pathway, dolomite may be primary or secondary. Primary dolomite is  
590 known to be microbially mediated at low temperatures (Bontognali et al., 2010; Zhang et al., 2015),



591 while secondary dolomite forms by the dolomitization process and is the diagenetic product of  
592 calcium carbonate minerals (Machel, 1978; Guido et al., 2018). Secondary dolomite starts by the  
593 formation of a metastable, non-stoichiometric magnesium calcium carbonate mineral phase from  
594 precursory calcite or aragonite minerals; this initial replacement starts with dissolution-re-  
595 precipitation and typically occurs in near-surface and shallow burial settings (Machel, 1978;  
596 Kupez et al., 1993; Gregg et al., 2015). Over time, and often in deeper burial setting,  
597 recrystallization of the non-stoichiometric mineral phases will form stable, stoichiometric  
598 dolomite phases (Machel, 1978; Kupez et al., 1993; Warren, 2000; Kaczmarek and Sibley, 2014;  
599 Gregg et al., 2015). Dolomite is considered stoichiometric and well-ordered when cations of  
600 magnesium and calcium reach a 1:1 ratio in alternating sheets within the carbonate crystal lattice  
601 (Machel, 1978). Therefore, secondary dolomite that is stoichiometric and has an ordered cation  
602 arrangement is considered to be diagenetically replaced, or, recrystallized. Although a recent study  
603 reported primary precipitation of stoichiometric and ordered dolomite from low temperature  
604 (27°C) using cultured anaerobic photosynthetic biofilm in conditions relevant to Archean seawater  
605 (Daye et al., 2019), stoichiometric and ordered dolomite has not yet been synthesized in the  
606 laboratory by abiotic, secondary dolomite precipitation at such low temperatures (Land, 1998;  
607 Gregg et al., 2015). Instead, the successful synthesis of secondary dolomite results from greater  
608 than 100°C (high) temperature experiments where the precursory calcium carbonate minerals  
609 undergo dissolution-re-precipitation to from disordered, high-magnesium calcitic phases before  
610 forming ordered dolomite (Kaczmarek and Sibley, 2014; Gregg et al., 2015). This ‘dolomite  
611 problem’ (Machel, 2004) leads to the hypothesis that massive beds of ordered, stoichiometric  
612 dolomite in the geologic record, are predominately the result of high temperature dolomitization  
613 of original calcitic carbonates. High temperatures dolomitization usually refers to greater than

614 100°C or 200°C (Kaczmarek and Sibley, 2014; Gregg, 2015), but temperatures as low as 50°C  
615 have been considered to be enough to alter original chemical signatures such as isotopic values  
616 and trace element concentrations (Gregg and Sibley, 1984; Warren, 2000). Even this type of low  
617 temperature dolomitization has been thought to alter original textural (Grotzinger and Knoll,  
618 1999), and chemical signatures (Gregg and Sibley, 1984; Allan and Wiggins, 1993; Machel, 1997,  
619 Warren, 2000; Gregg et al., 2015; Kaczmarek and Sibley, 2014), and therefore may not be  
620 favorable for the preservation of original organic chemistry or body fossils (Schopf, 1999).

621 Experimental work has shown that stoichiometry increases with increasing Mg/Ca ratios in the  
622 fluid, and ordering increases over the reaction time; indicating that stoichiometry is associated with  
623 Mg concentration in the formation fluid and cation ordering is associated with the length of  
624 reaction time (Kaczmarek and Sibley, 2011). Accordingly, the level of diagenetic replacement  
625 within secondary dolomite can be inferred by both the dolomite's stoichiometry and degree of  
626 cation ordering. Stoichiometric dolomite has values of 2.89 Å  $d_{104}$ -spacing and 0.6 Mg/Ca ratios,  
627 and cation ordering of 0.40 or greater indicates relatively well-ordered dolomite. The average XRD  
628  $d_{104}$ -spacing value for whole rock samples is 2.89 Å, which is indicative of stoichiometric dolomite  
629 (Table 1) (Goldsmith and Graf, 1958; Durocher and Al-Aasm, 1997). The average Mg/Ca ratio  
630 obtained for bulk carbonate is 0.53, and for each generation of dolomite 0.62. The degree of cation  
631 order in bulk rock samples ranges from 0.36 to 0.99, which indicates the samples are relatively  
632 well ordered and that the dolomitization was either a prolonged process (Kaczmarek and Sibley  
633 2011) or involved a concentrated Mg ion solution (Sijing et al., 2014).

634 The Allentown dolomite does not retain evidence of the non-stoichiometric metastable  
635 magnesium carbonate minerals that are presumed to have formed during the initial dolomitization  
636 stages of the limestone replacement. The XRD  $d_{104}$ -spacing, Mg/Ca ratio, and cation ordering

637 values (Table 1 and Fig. 4) are consistent and show that the Allentown dolomite from the analyzed  
638 outcrop is stoichiometric and ordered, and the original limestone formation has been entirely  
639 replaced by dolomite and fully recrystallized.

#### 640 *5.2.1. Multi-generational dolomite*

641 Petrographic features, luminescence, and microprobe analyses suggest multistage  
642 dolomitization. Dolomite petrography shows three texturally different crystal types that are  
643 compositionally different, as revealed by CL and EPMA analyses. Determining the order of  
644 dolomite crystal formation is essential to reconstruct the paragenetic sequence and to reveal if  
645 chemical, thermal, or textural overprinting by later crystal generations exists. The following  
646 sections discuss the interpreted formation of each generation of dolomite.

##### 647 *5.2.1.1. Microspar dolomite*

648 The first generation of dolomite is a finely crystalline replacive dolomite typified by microspar-  
649 sized crystals (Folk, 1959) with an average crystal size of 20 microns. This secondary dolomite  
650 replaced the precursory micritic limestone that formed by the lithification of calcium carbonate  
651 minerals from the original marginal marine depositional setting. Microcrystalline textures in  
652 dolomite (<10 microns) are thought to be from waters supersaturated in Mg (Sibley, 1991; Allan  
653 and Wiggins, 1993) and are common to early near surface dolomitization, and microbial-related  
654 primary dolomite precipitation (Moore, 1989; Sibley, 1991; Allan and Wiggins, 1993); The  
655 microspar dolomite reported here is larger in crystal size due to the coarsening of original  
656 microcrystalline calcium carbonate minerals during dolomitization (Folk, 1959). This generation  
657 of dolomite exhibits nonplanar, irregular intercrystalline grain boundaries, which is a common  
658 textural characteristic of growth at temperatures greater than 50°C (Gregg and Sibley, 1984; Sibley  
659 and Gregg, 1987; Warren, 2000), however, this texture has also been observed to form in low

660 temperature, subaerial environments in the presence of concentrated Mg ion solution which  
661 enables rapid nucleation of crystals during dolomitization (Sijing et al., 2014). Based on all other  
662 evidence that is in agreement with near surface, low temperature formation, the microspar  
663 dolomite's texture likely resulted from rapid crystal growth in the presence of concentrated Mg  
664 ion fluids.

665 The CL spectral peaks at 389 nm and 650 nm are due to intrinsic lattice defects in the  $\text{CO}_3^{2-}$   
666 structure and the substitution of  $\text{Mg}^{2+}$  with  $\text{Mn}^{2+}$  into the carbonate lattice, respectively (Machel  
667 et al., 1991; Habermann et al., 1997; Richter et al., 2003). A peak shift is present at 389 nm and  
668 may be due to different types of crystallographic lattice defects such as ion vacancies and other  
669 point defects. Variations in crystallographic defects may account for the variations in CL colors of  
670 increasing wavelength from blue, grey, to gold. Further, the three observed CL colors are found in  
671 the first two generations (microspar and zoned) of dolomite which are both interpreted to have  
672 formed in the early meteoric diagenetic realm, which may suggest that this luminescence pattern  
673 is related to the dolomite's formation path. Although rarely reported (Kusano et al. 2014), this  
674 violet-blue range of luminescence is known to occur in calcite and dolomite minerals that lack  
675 impurities (Machel et al., 1991), because the Allentown dolomite contains Si, Mn, Fe, and Zn  
676 impurities, the luminescence character is likely attributed to intrinsic crystallographic defects.

#### 677 *5.2.1.2. Zoned dolomite*

678 Zoned dolomite occurs as small rhombohedral shaped crystals that infill pore space within  
679 the microspar dolomite (Fig. 6 A), and larger cavity lining crystals with cloudy rhombic cores  
680 (Fig. 6 B). Although the rhombohedral dolomite may have precipitated directly from fluids  
681 saturated in Mg ions while the outcrop was subaerially exposed (Sibley, 1978), the presence of  
682 cloudy cores suggests later recrystallization. Preserved zonation in crystals is recorded stages of

683 primary crystal growth and relates to the fluctuating pore water chemistry during formation, a  
684 feature observed in dolomites formed during meteoric diagenesis (Allan and Wiggins, 1993).  
685 The zonation growth stages of primary precipitation alter between Ca:Mg zones that record  
686 mixed water influx likely from fresh and marine waters, to Fe:Mg zones that record reducing  
687 conditions from likely stagnant fluids (Katz, 1971). These growth stages may be related to the  
688 storm events recorded in bedding layers (see sections 2.2. and 5.1.) because only Fe<sup>2+</sup> is  
689 incorporated into the carbonate lattice by replacing the Mg<sup>2+</sup> in lattice sites (Katz, 1971; Allan  
690 and Wiggins, 1993); this oxidized state of Fe indicates that the dark bands of zonation formed  
691 during strong reducing conditions of stagnant fluids, and the light bands of zonation formed after  
692 storm events flushed the system and oxygenated the water leaving no soluble ferrous iron in  
693 solution, allowing the Ca:Mg zones to form (Katz, 1971).

694 The zoned dolomite exhibits the same CL characteristics as the microspar dolomite and may  
695 represent penecontemporaneous formation with the microspar dolomite, from the same type of  
696 meteoric fluids. Conversely, formational fluids may have interacted by causing minor dissolution  
697 of the microspar dolomite and released Mg and Si to be recycled into the zoned generation  
698 (Goodell and Garman, 1969; Land et al., 1975). Both scenarios could explain the Si present in  
699 the zoned dolomite, which is absent from the saddle dolomite.

#### 700 *5.2.1.3. Saddle dolomite*

701 Saddle dolomite occurs as void-filling centers in primary fenestral pores and secondary  
702 microfractures and vugs. The dull luminescence, Fe-rich chemistry and saddle shape are all  
703 features of late stage, high temperature dolomite formation (Allan and Wiggins, 1993). This  
704 dolomite phase may be primary precipitated or replacive, but the lack of calcite relics indicates it  
705 is a primary cavity-fill phase (Mehmood et al., 2018). Observational crosscutting evidence at the

706 outcrop is limited to one large saddle-filled vug that an overlying stylolite collapsed into and is  
707 surrounded by the infilling saddle dolomite (Fig. 2 Q). This suggests a penecontemporaneous  
708 formation of the two, and the saddle dolomite may have incorporated Mg from microspar dolomite  
709 after dissolution from stylolization during increasing overburden pressure that released Mg into  
710 the burial fluids (Goodell and Garman, 1969; Land et al., 1975). This Mg recycling could explain  
711 why stable oxygen isotope compositions overlap in all three generations of dolomite. The  
712 formational burial setting of saddle dolomite suggests it formed in a rock-buffered, isotopically  
713 closed system where pore fluids were, at least partially, composed of Mg provided from the  
714 penecontemporaneous dissolution of the host rock's microspar dolomite during localized  
715 stylolization (Gray et al., 1991; Oehlert and Swart, 2014) This final stage of dolomite formation  
716 thermally overprinted the entire formation as revealed from the light stable oxygen isotope  
717 composition (see 5.2.2.) and organic carbon Raman D and G bands (see 5.3.2.).

#### 718 5.2.2. Carbonate $\delta^{18}O$ and $\delta^{13}C$ composition

719 The positive covariance ( $r=0.87$   $n=15$  [bulk];  $r=0.96$   $n=3$  [microspar]) in  $\delta^{18}O$  and  $\delta^{13}C$   
720 values suggests dolomite formation in a mixing zone of  $^{18}O$  and  $^{13}C$ -enriched and  $^{18}O$  and  $^{13}C$ -  
721 depleted water sources (Allan and Matthews, 1982; Allan and Wiggins, 1993; Oehlert and Swart,  
722 2014). A comparison of results from the micro-drilled saddle and microspar samples shows that  
723 these values cannot be differentiated from bulk carbonate sample results as they fall within the  
724 range of error bars (Fig. 12). This may be due to the fact that the majority of the bulk sample is  
725 composed of microspar dolomite, and therefore the diagenetic trend of this dolomite phase  
726 dominates. The low  $\delta^{18}O_{dolo}$  values (-18.23‰ to -6.05‰ VPDB) are likely from the late stage  
727 saddle dolomite which formed in deeper burial (Allan and Wiggins, 1993; Haas et al., 2017; Al-  
728 Aasm and Crowe, 2018) and at higher temperatures than the microspar and zoned dolomite.

729 The low values of  $\delta^{13}\text{C}_{\text{dolo}}$  (Fig. 12) are from alteration during dolomitization and likely  
730 signifies the presence of organics in the system (Irwin et al., 1977; Schidlowski, 1988; Allan and  
731 Wiggins, 1993; Lamb et al., 2006).  $\delta^{13}\text{C}_{\text{dolo}}$  values of -6‰ VPDB indicate thoroughly altered  
732 isotopic compositions from diagenesis in open systems with high water:rock ratios (Lohmann,  
733 1988; Sharp, 2007).

734 Coupled  $\delta^{18}\text{O}_{\text{dolo}}$  and  $\delta^{13}\text{C}_{\text{dolo}}$  isotopes suggest that alteration for both the carbon and oxygen  
735 isotopes for all samples is contemporaneous and originates from the same source(s) (Fig. 13 B)  
736 (Des Marais et al., 1992; Jiang et al., 2012). The decoupled trends of  $\delta^{13}\text{C}_{\text{org}}$  with  $\delta^{18}\text{O}_{\text{dolo}}$  and  
737  $\delta^{13}\text{C}_{\text{dolo}}$  are likely related to diagenetic alteration and indicate the system was not rock buffered  
738 and does not retain the original  $\delta^{13}\text{C}_{\text{dolo}}$  signature (Grotzinger et al., 2011; Jiang et al., 2012;  
739 Oehlert and Swart, 2014). Supporting this is the interpretation that the microspar and zoned  
740 dolomite formed in an early diagenetic setting of meteoric dolomitization, which is an isotopically  
741 open system (Gregory et al., 1989) where large amounts of fluids interacted with the rock and  
742 shifted  $\delta^{13}\text{C}_{\text{dolo}}$  values to lighter values (Lohman, 1988; Sharp, 2007; Oehlert and Swart, 2014).  
743 Therefore, the decoupled  $\delta^{13}\text{C}_{\text{org}}$  and  $\delta^{13}\text{C}_{\text{dolo}}$  values indicate that diagenesis altered  $\delta^{13}\text{C}_{\text{dolo}}$  values  
744 during exposure to freshwater, and this high fluid to rock ratio is responsible for the decoupled  
745 signature (Grotzinger et al., 2011; Jiang et al., 2012; Oehlert and Swart, 2014).

### 746 **5.3. Characterization of organic carbon**

747 Organic carbon is characterized here using TOC,  $\delta^{13}\text{C}_{\text{org}}$ , Raman mapping, and D and G peak  
748 analyses to determine alteration setting, spatial relationships between organic matter and minerals,  
749 and thermal maturity.

#### 750 *5.3.1. TOC and $\delta^{13}\text{C}_{\text{org}}$*

751 The samples with higher TOC concentrations (0.484 to 0.286 wt %) have lighter  $\delta^{13}\text{C}_{\text{org}}$   
752 compositions, while samples with lower TOC (approximately 0.056 wt %) show heavier  $\delta^{13}\text{C}_{\text{org}}$   
753 compositions (Fig. 13 A). Such a decrease in TOC coupled with lighter  $\delta^{13}\text{C}_{\text{org}}$  values is indicative  
754 of post-depositional thermal degradation (McKirdy and Powell, 1974; Strauss and Beukes, 1996;  
755 Eigenbrode and Freeman, 2006; Jiang et al., 2012). Oolitic dolosiltite sample A9 has the highest  
756 TOC at 0.48 wt %; this sample is dark grey microspar dolomite associated with rip-up clasts. Rip-  
757 up clasts appear periodically throughout the outcrop and are indicative of tidal channel deposits  
758 which may have deposited during storm events. The increase in TOC within samples A9, and  
759 oolitic dolarenite samples A10, A11, and oolitic dolosiltite sample A13, all of which include high  
760 energy, storm evidence of rip-up clasts and edge-wise conglomerates, suggests the possibility of  
761 terrestrial organic input that washed in during storms and was incorporated in the sediments and  
762 stromatolitic laminae during deposition.

763 The values of  $\delta^{13}\text{C}_{\text{org}}$  range from -25.73 ‰ to -27.95 ‰ relative to VPDB (Fig. 13 B), which  
764 is consistent with organic input from decaying organic matter or microbial metabolism (Irwin et  
765 al., 1977; Schidlowski, 1988; Allan and Wiggins, 1993; Lamb et al., 2006)

### 766 5.3.2. Raman mapping and thermometry

767 The spatial relation of the organic carbon to multi-generational dolomite is significant for  
768 determining if the carbon was already in place before dolomitization, and therefore syngenetic  
769 with the Cambrian stromatolites. Confocal Raman microscopy reveals that D and G bands of  
770 organic carbon are only present in the first generation of dolomite and situated at or near grain  
771 boundaries.

772 The use of oxygen isotope ratios in carbonate minerals as a geothermometer (Friedman and  
773 O'Neil, 1977; Allan and Wiggins, 1993) is not justified here because measured oxygen isotopes



774 values and geochemical data indicates that dolomitization did not take place in marine settings,  
775 but rather meteoric and burial settings which had reset the isotopic seawater values. Additionally,  
776 the late stage burial dolomitization thermally overprinted previous generations, obliterating the  
777 original dolomitization temperature (Land, 1980; Sharp, 2007) of the microspar dolomite.  
778 Therefore, calculated formation temperatures using a Cambrian marine baseline would be  
779 erroneous for this sample set and not indicative of the maximum burial temperature.

780 However, the color alteration index (CAI) of conodont fossils has shown to be a useful  
781 geothermometer to determine thermal maturity in sedimentary rock (Epstein et al., 1977; Marshall  
782 et al., 2001). Harris et al. (1995) report few conodont fossils (1-10 elements per kilogram of rock)  
783 were found in Warren and Sussex counties of New Jersey Allentown outcrops and those were  
784 poorly preserved texturally, deformed and fractured. The conodont fossils found have CAI  
785 (Epstein et al., 1977; Helsen et al., 1995) values of 5 that indicate that the Allentown dolomite  
786 reached temperatures of at least 300°C and burial depths of at least 10 km (Harris et al., 1995).  
787 Burial depths around 10 km would indicate burial pressure was at least 300 MPa (Tilley, 1924).  
788 Based on our outcrop observations and microtextural evidence, this outcrop had not been exposed  
789 to unidirectional stress that would align or elongate grains, but the pressure was likely lithostatic  
790 and uniform pressure derived from the burial process. However, the burial pressure had likely  
791 created the vertical microfractures observed in some layers (see 4.2.2.) Similarly, Stead and  
792 Kodama (1984), reported that Pennsylvanian Allentown outcrops likely reached minimum  
793 temperatures of 200-300°C because younger, Ordovician rocks that had not been as deeply buried  
794 as the Allentown contain conodont fossils with CAI values of 3.5-5. Although there may exist  
795 regional differences in tectonic settings that operated between Pennsylvania and New Jersey or  
796 different stratigraphic levels of the Allentown formation that were sampled in those studies

797 compared to this study, the use of conodonts as a geothermometer for the dolomitization of the  
798 Allentown is useful and comparable to the Raman thermometry method used in this paper.

799 Organic carbon first-order bands of Raman spectra, (D and G bands at  $\sim 1350$  and  $1600\text{ cm}^{-1}$ ,  
800 respectively) record the host rock's maximum temperature and can be used as an organic  
801 paleothermometer (Pasteris and Wopenka, 1991; Wopenka and Pasteris, 1993; Marshall et al.,  
802 2001; Marshall et al., 2012). The G band is the ordered, graphitic structure of carbon, and the D  
803 band is the disordered carbon structure. Variations in the bands, related to differing amounts of  
804 thermally induced rearrangement, can be used to determine structural order of the carbon and  
805 associated temperature setting required for such level of crystallinity (Pasteris and Wopenka,  
806 1991; Beyssac et al., 2002). Although there is currently no agreement on how to process peak data  
807 for thermometry studies, the geothermometer from Kouketsu et al. (2014) were used to compare  
808 results to the maximum alteration temperature inferred from previous conodont studies and  
809 determine if a similar thermal alteration between the host rock and organics exists.

810 Calculated temperatures yield a range of  $300^{\circ}\text{C}$  -  $373^{\circ}\text{C}$  ( $\pm 30^{\circ}\text{C}$ ) which places the Allentown  
811 organic carbon within the medium-grade carbonaceous material temperature alteration zone of  
812  $280^{\circ}\text{C}$  -  $400^{\circ}\text{C}$ . This medium-grade type of organic carbon alteration is also reflected in the overall  
813 D and G band spectral characteristics which exhibit D3 and D4 bands, and commonly have D and  
814 G bands that are equal in intensity (Table 2 and Tables 3a and 3b in supplementary material).  
815 These derived temperatures from collected Raman data corroborate the same temperature of  
816 thermal alteration as the dolomitization setting previously established using the conodont fossil  
817 CAI geothermometer.

818 *5.3.3. Syngenicity and Indigeneity*

819 Based on the spatial association with dolomite grains, and exclusive occurrence in the replacive  
820 microspar dolomite, the organic carbon was likely in place during dolomitization -previously  
821 trapped during the original limestone lithification (Fig. 15 B and Fig. S3 in supplementary  
822 material). This early dolomitization likely occurred penecontemporaneously with the lithification  
823 of limestone, from fluids supersaturated in Mg ions from seawater and freshwater mixing, that it  
824 rapidly produced stoichiometric dolomite, which as a thermodynamically stable phase, resisted  
825 further alteration and preserved the Cambrian organics by basically locking the first generation to  
826 prevent later fluid contaminations from entering. The placement of organic carbon suggests it is  
827 indigenous and syngenetic to the primary fabric of the host rock. The Raman cluster maps show  
828 the peak variations overlap spatially, suggesting all three varieties of organics were in place at the  
829 same time and the matching the alteration temperature with the host rock. All of these  
830 characteristics indicate that organic molecules are indigenous and syngenetic to the Cambrian  
831 dolomitic stromatolites.

#### 832 *5.3.4. Biogenicity*

833 Claims of biogenicity of organic carbon unrelated to cellular morphological evidence should  
834 be approached with caution. The finding of organic carbon with an isotopic composition that may  
835 be indicative of microbial metabolism is not an explicit line of evidence for biogenicity (Braiser  
836 et al., 2003; De Gregorio and Sharp, 2006). Organic molecules can form from abiotic,  
837 autochthonous chemical reactions such as Fischer-Tropsch type processes in hydrothermal  
838 environments and decarbonation during metamorphism (McCollom and Seewald, 2006; Galvez et  
839 al., 2013; Bernard and Papineau, 2014). Although this null hypothesis cannot be fully rejected,  
840 there is no evidence of such hydrothermal processes in the outcopping area; and such a formational

841 pathway was not likely present in this ancient coastal setting where it is interpreted that early  
842 dolomitization took place and preserved the organic carbon.

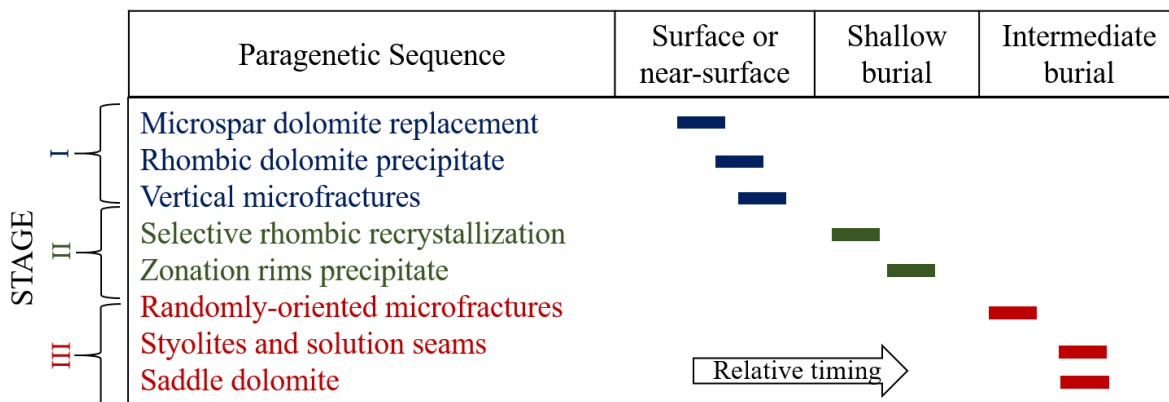
843 The evidence for Allentown organic carbon deriving from a biogenic origin are: 1) organic  
844 carbon is exclusive to the primary fabric (microspar dolomite) of the host rock which indicates a  
845 syngenetic origin, 2) the geological context is a marginal-marine setting with numerous microbial  
846 stromatolite macrostructures, 3) geochemical signals of  $\delta^{13}\text{C}_{\text{org}}$  values are indicative of biology,  
847 and although the detection of disordered carbon by Raman spectroscopy is not alone indicative of  
848 biogenicity (Pasteris and Wopenka, 2003), the variations within D and G bands may be indicative  
849 of various alteration levels due to different types of starting material, of which one of more phases  
850 may be biological in origin.

851 The D and G peak differences may be due to different types of organic starting material that  
852 altered, or decomposed, differently despite undergoing the same alteration setting (Lamb et al.,  
853 2006). As an example, Lamb et al. (2006) reported organic matter in Holocene lagoonal and tidal  
854 flat sediments is mostly derived from suspended particulate organic matter such as plant detritus  
855 and phytoplankton from river and marine sources, respectively. Specifically, tidal flats are  
856 composed of a balanced mix between in situ organics and organics transported in by tides or rivers,  
857 both due to regular flushing or mixing of fresh and marine waters; lagoons are dominated by in  
858 situ organic sources due to isolation of waters (Lamb et al., 2006). This variation in tidal flat  
859 organics may potentially explain how three phases of organic carbon are found in the microbial  
860 samples (A16 and A5) and the lagoonal (A7) and ooid (A11 and A12) samples only have one  
861 carbon phase present (Fig. 14, Fig. 15, and Fig. S3 in supplementary material).

## 862 **5.4. Paragenetic Sequence**

### 863 *5.4.1. Relative timing of dolomitization stages*

864 Three stages of diagenesis have been outlined to explain the diagenetic phases observed in the  
 865 Allentown Formation (Fig. 16). During stage 1, the Allentown Formation was deposited during  
 866 the Late Cambrian in a transitional marginal marine setting. Facies produced in this peritidal  
 867 environment range from thinly-laminated stromatolitic, fine-grained lagoonal thrombolite, and  
 868 massive oolitic grainstones. At the time of deposition, micritization of calcium carbonate grains  
 869 during lithification of limestone occurred. The limestone dolomitized early in the marginal marine  
 870 setting where freshwater mixed with marine water and produced microspar dolomite. Occurring  
 871 contemporaneously, primary precipitation of dolomite rhombs that infill interparticle pores of  
 872 microspar dolomite. During stage 2, increasing burial depth leads to microfracturing in selected  
 873 layers of microspar dolomite, and recrystallization of some rhombic dolomite crystals. Mixed  
 874 meteoric-marine fluids, alternating between oxidized and reduced conditions, produce zoned  
 875 dolomite rims, while the original limestone is likely now completely dolomitized and  
 876 stoichiometric. During stage 3, deeper burial produced late stage chemical compaction from  
 877 overburden pressure resulting in stylolites, and localized dissolution seams that are concentrated  
 878 in the lagoonal facies layers. A second stage of microfracturing occurs in select layers. Void filling  
 879 dolomite precipitates in vugs, fractures, and fenestral pores by Fe- and Mn- rich, and likely  
 880 reducing fluids.



881 **Fig. 16.** Paragenetic sequence showing the formation of each dolomite generation with  
 882 increasing burial depth. Modified from Hips et al. (2015).

883

884 *5.4.2. Early dolomitization and preservation of organic carbon*

885       Based on the mineral stoichiometry and cation ordering, the Allentown dolomite is completely  
886 recrystallized (Machel, 1978; Kupecz et al., 1993; Kaczmarek and Sibley, 2014; Gregg et al.,  
887 2015). The increase in Fe and Mn with each dolomite generation, undetectable Sr and Na  
888 concentrations, along with nonplanar crystal boundaries within microspar and saddle dolomite,  
889 zonation within the second generation, and saddle-shaped crystals within the third generation, all  
890 provide excellent evidence of the order and manner in which dolomitization process developed  
891 (Machel, 1978; Kupecz et al., 1993; Kaczmarek and Sibley, 2014; Gregg et al., 2015). The three  
892 generations of dolomite, although all subjected to the maximum burial temperature average of  
893 331°C, preserved changes in the dolomitizing setting's fluid chemistry, which is apparent in CL  
894 color and EPMA spot analysis (see 5.2.1.).

895       A possible scenario for the Allentown's dolomitization and the relative timing of the  
896 development of each dolomite generation is presented here. Organic carbon is detected only within  
897 the first generation of microspar dolomite, at or near grain boundaries, and altered under similar  
898 burial and thermal conditions as the host rock. Organic material trapped in carbonate sediments  
899 during lithification will be displaced as the carbonate crystals grow larger and push organics  
900 between grain boundaries; thus, the organic carbon mapped was likely in place during the original  
901 lithification of limestone and before the microspar dolomite grains formed. The zoned dolomite  
902 precipitated directly from solution by infilling pore spaces within the microspar dolomite, and it  
903 exhibits the same luminescence of the microspar generation, suggesting this generation of dolomite  
904 may have precipitated penecontemporaneously with the microspar dolomite. As burial increased,  
905 temperature and pressure increased, and fluid chemistry changed to reflect Fe- and Mn-

906 enrichment, recrystallizing the rhombohedral cores of the second dolomite generation before  
907 further precipitating outward in zonation rims of altering formation fluid, which remained  
908 preserved even during deeper burial and higher temperatures. The dull luminescence from the third  
909 generation of saddle dolomite differs from the first two dolomite generations and marks a different  
910 formational setting at a deeper burial, higher temperatures, and likely more reducing fluid  
911 signatures of elevated Fe- and Mn- trace elements in the dolomite lattice. The formation of the  
912 microspar and zoned dolomite led to decreased porosity of the host rock, which made the host rock  
913 impermeable to the later, deeper burial, and possibly hydrothermal in origin (Machel and Lonnee,  
914 2002), saddle dolomite phase, and although thermally overprinted, did not chemically or  
915 structurally alter the microspar and zoned dolomite generations.

916 Stoichiometric dolomite is a thermodynamically stable phase of dolomite (Nordeng and Sibley,  
917 1994) that is less susceptible to alteration by later diagenesis (Mueller et al., 2019). It is possible  
918 that the microspar and zoned dolomites were stoichiometric and thermodynamically stable before  
919 the formation of saddle dolomite and thus not susceptible to, further, deeper burial dolomitization.  
920 The sealing of the first microspar generation of dolomite by the second zoned generation of  
921 dolomite may be the reason why the organic carbon has remained preserved since the Cambrian.

922

## 923 **6. CONCLUSIONS**

924 Secondary, stoichiometric and ordered dolomite has been hypothesized to occur at either  
925 high temperatures or from multiple stages of recrystallization (Machel, 1978; Kupecz et al.,  
926 1993; Gregg et al., 2015) that would likely erase evidence of original texture, chemistry, and  
927 biology (Gregg and Sibley, 1984; Grotzinger and Knoll, 1999; Schopf, 1999; Warren, 2000). The  
928 results presented here indicate that stoichiometric and ordered dolomite can form within early

929 dolomitization settings, undergo increasing temperature and burial diagenesis, and still retain  
930 syngenetic organic carbon. In summary:

- 931 • Outcrop observations (mudcracks, collapse breccia, rip-up clasts, edge-wise conglomerates)  
932 and petrological characteristics (finely-laminated stromatolites, fenestral porosity, rip-up  
933 clasts, finely crystalline microspar dolomite) reveal that the Allentown depositional setting was  
934 a tidal flat along the Cambrian coastline where original calcium carbonate mineral precursors  
935 dolomitized early in a marginal marine setting.
- 936 • The dolomite is ordered and all three generations of dolomite are stoichiometric and, therefore,  
937 fully recrystallized.
- 938 • Geochemical characteristics recorded by each generation of dolomite suggests two  
939 dolomitization processes dominated, mixing zone dolomitization in the meteoric diagenesis  
940 realm and burial dolomitization in the burial diagenesis realm.
- 941 • Microspar and zoned dolomite generations formed by dolomitization in a marine-meteoric  
942 mixing zone as revealed by the absence of evaporitic minerals and the presence of finely  
943 crystalline replacive dolomite crystals, as well as undetectable Sr and Na, and covariance in  
944  $\delta^{13}\text{C}_{\text{dolo}}$  and  $\delta^{18}\text{O}_{\text{dolo}}$  values. Saddle dolomite formed by burial dolomitization as revealed by  
945 coarse void-filling crystals, dull luminescence, Fe and Mn enrichment, and low  $\delta^{18}\text{O}_{\text{dolo}}$  values.
- 946 • The microspar and zoned dolomite were thermally overprinted by saddle dolomite during  
947 burial diagenesis. However, it did not overprint the formational chemistry of the previous two  
948 dolomite generations, suggesting that the burial was intermediate depth and temperatures and  
949 pressures were not high enough to obliterate previous generational dolomite that was likely  
950 stoichiometric and therefore thermodynamically stable, and not reactive to this final stage of  
951 diagenesis.



952 • Raman D and G bands indicate greenschist-like thermal maturity of organic carbon within the  
953 formation which is also suggested by conodont fossil CAI geothermometry from previous  
954 formational temperature studies of the Allentown dolostone.

955 • Organic carbon is found at or near grain boundaries, and only within the first generation of  
956 microspar dolomite. This suggests the organics were in place when the grains of dolomite  
957 formed, indicating a syngenetic origin of the organic carbon within the Cambrian stromatolites

958 Carbonate lithologies are diagenetically complex and their depositional and diagenetic setting  
959 will directly influence what biosignatures are preserved. This study reveals that dolomite that has  
960 undergone greenschist facies style thermal alteration can still retain original geochemical  
961 signatures necessary to reconstruct paragenesis, which along with outcrop observations,  
962 petrography, and Raman microscopy allows for the determination of biosignature syngeneticity  
963 within ancient stromatolites that have been entirely diagenetically replaced by secondary  
964 dolomitization. The importance of this study is that preserved organic signatures, without cellular  
965 morphological support, can be used to determine syngeneticity with host rock and open discussion  
966 for indigenous and biogenetic origins. This type of research is especially important when  
967 searching for life on other planets because microbial fossil preservation on Earth is rare, and  
968 different geologic environments and evolutionary histories on other planetary bodies will likely  
969 result in different types of life signatures recorded in the rocks. Terrestrial analogs such as this  
970 study will allow for better interpretations of potential biosignatures in Martian carbonates, which  
971 may have undergone varying levels of alteration. The Mars Perseverance Rover has the ability to  
972 target fine-grained carbonate rock, such as the microspar dolomite in this study, for Raman  
973 analysis, and if carbon is detected, these may serve as high potential biosignatures to be cached  
974 for future sample return mission(s).

975 **7. ACKNOWLEDGMENTS**

976 We are grateful to Alexander Gates and Michael Kalczynski for their assistance with field trip  
977 logistics and sample collection. This study was funded by NASA ASTEP (NNX14AT28G to  
978 M.G.) and NASA NAI ENIGMA – Rutgers University (80NSSC18M0093). The ICP-OES  
979 instrumentation used was purchased by NSF MI grant (EAR-1530582 to Ashaki Rouff). We thank  
980 Suah Yekeh for ICP-OES sample processing and data collection, supported by NSF REU (NSF-  
981 1459228 to Alexander Gates).

982 **8. DATA AVAILABILITY**

983 Supplementary data related to this article can be found at  
984 <http://dx.doi.org/10.17632/k57gbw78d9.1>, hosted at Mendeley Data (Murphy et al., *subm*).

985 **9. REFERENCES**

- 986 Al-Aasm, I. S., Crowe, R. 2018. Fluid compartmentalization and dolomitization in the Cambrian  
987 and Ordovician successions of the Huron Domain, Michigan Basin. *Mar. Petrol. Geol.* 92, 160-  
988 178.
- 989 Allan, J. R., Matthews, R. K. 1982. Isotope signatures associated with early meteoric diagenesis.  
990 *Sedimentology* 29, 797-817.
- 991 Allan, J. R., Wiggins, W. D. 1993. Dolomite reservoirs: geochemical techniques for evaluating  
992 origin and distribution, AAPG Continuing Education Course Notes No. 36.
- 993 Allwood, A. C., Walter, M. R., Kamber, B. S., Marshall, C. P., Burch, I. W. 2006. Stromatolite  
994 reef from the Early Archaean era of Australia. *Nature* 441, 714-718.
- 995 Ayllón-Quevedo, F., Souza-Egipsy, V., Sanz-Montero, M. E., Rodríguez-Aranda, J. P. 2007. Fluid  
996 inclusion analysis of twinned selenite gypsum beds from the Miocene of the Madrid basin  
997 (Spain). Implication on dolomite bioformation. *Sed. Geol.* 201, 212-230.

- 998 Barghoorn, E. S. Tyler, S. A. 1965. Microorganisms from the Gunflint Chert: These structurally  
999 preserved Precambrian fossils from Ontario are the most ancient organisms known. *Science*  
1000 147, 563-75.
- 1001 Bartley, J. K., Knoll, A. H., Grotzinger, J. P., Sergeev, V. N. 2000. Lithification and fabric genesis  
1002 in precipitated stromatolites and associated peritidal carbonates, Mesoproterozoic Billyakh  
1003 Group, Siberia, in: Grotzinger, J. P., James, M. P. (Eds.), *Carbonate Sedimentation and*  
1004 *Diagenesis in the Evolving Precambrian World*. SEPM Spec. Publ. 67, 59-73.
- 1005 Bernard, S. Papineau, D. 2014. Graphitic Carbons and Biosignatures. *Elements* 10, 435-440.
- 1006 Beyssac, O., Goffe, B., Chopin, C., Rouzaud, J. N. 2002. Raman spectra of carbonaceous material  
1007 in metasediments: a new geothermometer. *J. Metamorphic Geol.* 20, 859-871.
- 1008 Bontognali, T. R. R., Vasconcelos, C., Warthmann, R. J., Bernasconi, S. M., Dupraz, C.,  
1009 Strohmenger, C. J., McKenzie, J. A. 2010 Dolomite formation within microbial mats in the  
1010 coastal sabkha of Abu Dhabi (United Arab Emirates). *Sedimentology* 57(3), 824-844.
- 1011 Bragg, W. H. Bragg W. L. 1913. The Reflection of X-rays by Crystals. *Proceedings of the Royal*  
1012 *Society of London. Series A, Containing Papers of a Mathematical and Physical Character*  
1013 88(605), 428-438.
- 1014 Braiser, M., Green, O., Lindsay, J., Steele, A. 2003. Earth's oldest (~3.5 Ga) Fossils and the 'Early  
1015 Eden Hypothesis': Questioning the Evidence. *Origins Life Evol. Biosph.* 34, 257-269.
- 1016 Braiser, M. D., Antcliffe, J., Saunders, M., Wacey, D. 2015. Changing the picture of Earth's  
1017 earliest fossils (3.5–1.9 Ga) with new approaches and new discoveries. *PNAS* 112, 4859.
- 1018 Buick, R. 1990. Microfossil Recognition in Archean Rocks: An Appraisal of Spheroids and  
1019 Filaments from a 3500 M.Y. Old Chert-Barite Unit at North Pole, Western Australia. *Palaios*  
1020 5(5), 441-459.

- 1021 Buie, B. F. 1932. A Report of Investigations of the Allentown Limestone Formation. Thesis.  
1022 LeHigh University, PA.
- 1023 Calça, C. P., Fairchild, T. R., Cavalazzi, B., Hachiro, J., Petri, S., Huila, M. F. G., Toma, H.E.,  
1024 Araki, K. 2016. Dolomitized cells within chert of the Permian Assistência Formation, Paraná  
1025 Basin, Brazil. *Sed. Geol.* 335, 120-135.
- 1026 Dalton, R. F., Volkert, R. A., Monteverde, D. H., Herman, G. C., Canace, R. J. 2014. Bedrock  
1027 Geologic Map of the Hamburg Quadrangle, Sussex County, New Jersey (1:24,000), New  
1028 Jersey Geological and Water Survey, Trenton, NJ.
- 1029 Daye, M., Higgins, J., Bosak, T. 2019. Formation of ordered dolomite in anaerobic photosynthetic  
1030 biofilms. *Geology* 47(6), 509–512.
- 1031 De Gregorio, B. T. Sharp, T. G. 2006. The structure and distribution of carbon in 3.5 Ga Apex  
1032 chert: Implications for the biogenicity of Earth's oldest putative microfossils. *Amer. Miner.*  
1033 91, 784-789.
- 1034 Des Marais, D. J., Strauss, H., Summons, R. E., Hayes, J. M. 1992. Carbon isotope evidence for  
1035 the stepwise oxidation of the Proterozoic environment. *Nature* 359, 605-609.
- 1036 Drake Jr., A. A. 1965. Carbonate Rocks of Cambrian and Ordovician Age Northampton and Bucks  
1037 Counties, Eastern Pennsylvania and Warren and Hunterdon Counties, Western New Jersey.  
1038 *Bull. US Geol. Surv.* 1194-L.
- 1039 Durocher, S. Al-Aasm, I. 1997. Dolomitization and Neomorphism of Mississippian (Visean)  
1040 Upper Debolt Formation, Blueberry Field, Northeastern British Columbia: Geologic,  
1041 Petrologic, and Chemical Evidence. *AAPG Bull.* 81(6), 954-977.
- 1042 Ehlmann, B. L., Mustard, J. F., Murchie, S. L., Poulet, F., Bishop, J. L., Brown, A. J., Calvin, W.  
1043 M., Clark, R. N., Des Marais, D. J., Milliken, R. E., Roach, L. H., Roush, T. L., Swayze, G.

- 1044 A., Wray, J. J. 2008. Orbital Identification of Carbonate-Bearing Rocks on Mars. *Science*  
1045 322(5909), 1828-1832.
- 1046 Eigenbrode, J. L. Freeman, K. H. 2006. Late Archean rise of aerobic microbial ecosystems. *PNAS*  
1047 103(43), 15759-15764.
- 1048 Epstein, A. G., Epstein, J. B., Harris, L. D. 1977. Conodont Color Alteration – an Index to Organic  
1049 Metamorphism. US Geol. Surv. Professional Paper 995.
- 1050 Flügel, E. 2004. Carbonate Depositional Environments, in: *Microfacies of Carbonate Rocks*.  
1051 Springer, Berlin, Heidelberg.
- 1052 Folk, R. L. 1959. Practical petrographic classification of limestones. *Bull. Amer. Assoc. Petrol.*  
1053 *Geol.* 43(1), 1-38.
- 1054 Friedman, I. O’Neil, J. R. 1977. Compilation of stable isotope fractionation factors of geochemical  
1055 interest. US Geol. Surv. Professional Paper 440-KK.
- 1056 Galvez, M. E., Beyssac, O., Martinez, I., Benzerara, K., Chaduteau, C., Malvoisin, B., Malavieille,  
1057 J. 2013. Graphite formation by carbonate reduction during subduction. *Nature Geoscience* 6,  
1058 473-477.
- 1059 Ganai, J. A., Rashid, S. A., Romshoo, S. A. 2018. Evaluation of terrigenous input, diagenetic  
1060 alteration, and depositional conditions of Lower Carboniferous carbonates of Tethys  
1061 Himalaya, India. *SESCI* 3, 33-49.
- 1062 Gasparrini, M., Bechstädt, T. Boni, M. 2006. Massive hydrothermal dolomites in the southwestern  
1063 Cantabrian Zone (Spain) and their relation to the Late Variscan evolution. *Mar. Petroleum*  
1064 *Geol.* 23, 543–568.
- 1065 Goldsmith, J. R., Graf, D. L. 1958. Relation between lattice constants and composition of the Ca-  
1066 Mg carbonate. *Am. Mineral.* 43, 84-101.

- 1067 Goodell, H. G., Garman, R. K. 1969. Carbonate geochemistry of Superior deep test well, Andros  
1068 Island, Bahamas. AAPG Bull. 53, 513-536.
- 1069 Goudge, T. A., Mustard, J. F., Head, J. W., Fassett, C. I., Wiseman, S. M. 2015. Assessing the  
1070 mineralogy of the watershed and fan deposits of the Jezero crater paleolake system, Mars. J.  
1071 Geophys. Res. 120, 775-808.
- 1072 Graf, D. L., Goldsmith, J. R. 1956. Some Hydrothermal Syntheses of Dolomite and Protodolomite.  
1073 J. Geol. 64(2), 173-186.
- 1074 Gray, D. R., Gregory, R. T., Durney, D. W. 1991. Buffered Fluid-Rock Interaction in Deformed  
1075 Quartz-Rich Turbidite Sequences, Eastern Australia. J. Geophys. Res. 96(B12), 19,681-  
1076 19,704.
- 1077 Gregg, J. M., Sibley, D. F. 1984. Epigenetic dolomitization and the origin of xenotopic dolomite  
1078 texture. J. Sediment. Petrol. 54, 908-931.
- 1079 Gregg, J. M., Bish, D. L., Kaczmarek, S. E., Machel, H. G. 2015. Mineralogy, nucleation and  
1080 growth of dolomite in the laboratory and sedimentary environment: A review. Sedimentology  
1081 62, 1749-1769.
- 1082 Gregory, R. T., Criss, R. E., Taylor Jr., H. P. 1989. Oxygen isotope exchange kinetics of mineral  
1083 pairs in closed and open systems: Applications to problems of hydrothermal alteration of  
1084 igneous rocks and Precambrian iron formations. Chem. Geol. 75(1-2), 1-42.
- 1085 Grotzinger, J. P., Rothman, D. H. 1996. An abiotic model for stromatolite morphogenesis. Nature  
1086 383, 423-425.
- 1087 Grotzinger, J. P., Knoll, A. H. 1999. Stromatolites in Precambrian Carbonates: Evolutionary  
1088 Mileposts or Environmental Dipsticks? Annu. Rev. Earth Planet. Sci. 27, 313-358.

- 1089 Guido, A., Russo, F., Miriello, D., Mastandrea, A. 2018. Autochthonous Micrite to  
1090 Aphanodolomite: The Microbialites in the Dolomitization Process, *Geosciences* 8, 451.
- 1091 Haas, J., Hips, K., Bundai, T., Gyori, O., Lukoczki, G., Kele, S., Demeny, A., Poros, Z. 2017.  
1092 Processes and controlling factors of polygenetic dolomite formation in the Transdanubian  
1093 Range, Hungary: a synopsis. *Int. J. Earth Sci.* 106, 991-1021.
- 1094 Habermann, D., Götze, J., Neuser, R., Richter, D.K. 1997. The phenomenon of intrinsic  
1095 cathodoluminescence: Case studies of quartz, calcite and apatite. *Zentralbl Geol Paläont Teil*  
1096 1, Heft 10–12, 1275–1284.
- 1097 Harris, A. G., Repetski, J. E., Stamm, N. R., Weary, D. J. 1995. Conodont Age and CAI Data for  
1098 New Jersey. *US Geol. Surv. Open-File Report* 95-557.
- 1099 Helsen, S., David, P., Fermont, W. J. J. 1995. Calibration of Conodont Color Alteration Using  
1100 Color Image Analysis. *J. Geol.* 103, 257-267.
- 1101 Hips, K., Haas, J., Poros, Z., Kele, S., Budai, T. 2015. Dolomitization of Triassic microbial mat  
1102 deposits (Hungary): Origin of microcrystalline dolomite. *Sed. Geol.* 318(1), 113-129.
- 1103 Horgan, B. H. N., Anderson, R. B., Dromart, G., Amador, E. S., Rice, M. S. 2020. The mineral  
1104 diversity of Jezero crater: Evidence for possible lacustrine carbonates on Mars. *Icarus* 339.
- 1105 Howell, B. F. 1945. Revision of Upper Cambrian faunas of New Jersey, *Geological Society of*  
1106 *America, Memoir* 12.
- 1107 Hu, C., Huang, J., Fang, N., Xie, S., Henderson, G. M., Cai, Y. 2005. Adsorbed silica in stalagmite  
1108 carbonate and its relationship to past rainfall. *Geochim. Cosmochim. Acta* 69(9), 2285-2292.
- 1109 Irwin, H., Curtis, C., Coleman, M. 1977. Isotopic evidence for source of diagenetic carbonates  
1110 formed during burial of organic-rich sediments. *Nature*, 269.

- 1111 Jiang, G., Wang, X., Shi, X., Xiao, S., Zhange, S., Dong, J. 2012. The origin of decoupled  
1112 carbonate and organic carbon isotope signatures in the early Cambrian (ca. 542-520 Ma)  
1113 Yangtze platform. *Earth Planet Sci Lett.* 317-318, 96-110.
- 1114 Kaczmarek, S. E., Sibley, D. F. 2011. On the evolution of dolomite stoichiometry and cation order  
1115 during high-temperature synthesis experiments: An alternative model for the geochemical  
1116 evolution of natural dolomites. *Sed. Geol.* 240(1-2), 30-40.
- 1117 Kaczmarek, S. E., Sibley, D. F. 2014. Direct physical evidence of dolomite recrystallization.  
1118 *Sedimentology* 61, 1862-1882.
- 1119 Katz, A. 1971. Zoned Dolomite Crystals. *J. Geol.* 79(1), 38-51.
- 1120 Kirmaci, M. Z., Akdağ, K. 2005. Origin of dolomite in the Late Cretaceous-Paleocene limestone  
1121 turbidites, eastern Pontides, Turkey. *Sed. Geol.* 181(1-2), 39-57.
- 1122 Knoll, A. H. Strother, P. K., Rossi, S. 1988. Distribution and Diagenesis of Microfossils from the  
1123 Lower Proterozoic Duck Creek Dolomite, Western Australia. *Precamb. Res.* 38, 257-279.
- 1124 Kouketsu, Y., Mizukami, T., Mori, H., Endo, S., Aoya, M., Hara, H., Nakamura, D., Wallis, S.  
1125 2014. A new approach to develop the Raman carbonaceous material geothermometer for low-  
1126 grade metamorphism using peak width. *Island Arc* 23, 33-50.
- 1127 Kupecz J. A., Montanez I. P., G., Gao 1993. Recrystallization of Dolomite with Time, in: Rezak,  
1128 R., Lavoie, D. L. (Eds.), *Carbonate Microfabrics. Frontiers in Sedimentary Geology.* Springer,  
1129 New York, NY.
- 1130 Kusano, N., Nishido, H., Inoue, K. 2014. Cathodoluminescence of calcite decomposed from  
1131 dolomite in high-temperature skarn. *J. Miner. Petrol. Sci.* 109(6), 286-290.
- 1132 Lamb, A. L., Wilson, G. P., Leng, M. J. 2006. A review of coastal palaeoclimate and relative sea-  
1133 level reconstructions using  $\delta^{13}\text{C}$  and C/N ratios in organic material. *Earth Sci. Rev.* 75, 29-57.



- 1134 Land, L. S., Salem, M. R. I., Morrow, D. W. 1975. Paleohydrology of Ancient Dolomites:  
1135 Geochemical Evidence. AAPG Bull. 59(9), 1602-1625.
- 1136 Land, L. S. 1980. The isotopic and trace element geochemistry of dolomite: The state of the art,  
1137 in: Zenger, D. H., Dunham, J. B., Ethington, R. L. (Eds.), Concepts and Models of  
1138 Dolomitization. SEPM Spec. Publ. 28, 87-110.
- 1139 Land, L.S. 1998. Failure to precipitate dolomite at 25°C from dilute solution despite 1000-fold  
1140 oversaturation after 32 years. Aquat. Geochem. 4(3- 4), 361–368.
- 1141 Li, Q., Jiang, Z., Hu, W., You, X. 2015. Origin of Dolomite in the Middle Triassic Zhouchongcun  
1142 Formation, Central Lower Yangtze Region, Southeast China. Carpath. J. Earth Env. 10(1), 89-  
1143 100.
- 1144 Lindtke, J., Ziegenbalg, S. B., Brunner, B., Rouchy, J. M., Pierre, C., Peckmann, J. 2011.  
1145 Authigenesis of native sulphur and dolomite in a lacustrine evaporitic setting (Hellín basin,  
1146 Late Miocene, SE Spain). Geol. Mag. 148(4), 655-669.
- 1147 Lohmann, K. C. 1988. Geochemical patterns of meteoric diagenetic systems and their application  
1148 to studies of paleokarst, in: James, N. P., Choquette, P. W. (Eds.), Paleokarst. Springer-Verlag,  
1149 New York, 58–80.
- 1150 Machel, H. G. 1978. Dolomites and dolomitization, in: Sedimentology. Encyclopedia of Earth  
1151 Science. Springer, Berlin, Heidelberg.
- 1152 Machel, H. G., Mason, R. A., Mariano, A. N., and Mucci, A. 1991. CAUSES AND EMISSION  
1153 OF LUMINESCENCE IN CALCITE AND DOLOMITE, in: Barker, C. E., Kopp, O. C. (Eds.),  
1154 Luminescence Microscopy and Spectroscopy: Qualitative and Quantitative Applications.  
1155 SEPM Short Course Notes, 25.

- 1156 Machel, H. G. 1997. Recrystallization versus neomorphism, and the concept of ‘significant  
1157 recrystallization’ in dolomite research. *Sed. Geol.* 113, 161-168.
- 1158 Machel, H. G., Lonnee, J. 2002. Hydrothermal dolomite – a product of poor definition and  
1159 imagination. *Sed. Geol.* 152(3-4), 163-171.
- 1160 Machel, H. G. 2004. Concepts and models of dolomitization – a critical reappraisal, in:  
1161 Braithwaite, C. J. R., Rizzi, G., Darke, G. (Eds.), *The Geometry and Petrogenesis of Dolomite*  
1162 *Hydrocarbon Reservoirs.* Geol. Soc. London, Spec. Publ. 235, 7-63.
- 1163 Marshall, A. O., Emry, J. R., Marshall, C. P. 2012. Multiple Generations of Carbon in the Apex  
1164 Chert and Implications for Preservation of Microfossils. *Astrobiology* 12(2).
- 1165 Marshall, C. P., Mar, G. L., Nicoll, R. S., Wilson, M. A. 2001. Organic geochemistry of artificially  
1166 matured conodonts. *Org. Geochem.* 32, 1055-1071.
- 1167 McCollom, T. M., Seewald, J. S. 2006. Carbon isotope composition of organic compounds  
1168 produced by abiotic synthesis under hydrothermal conditions. *Earth Planet Sci Lett.* 243, 74-  
1169 84.
- 1170 McKirdy, D. M., Powell, T. G. 1974. Metamorphic Alteration of Carbon Isotopic Composition in  
1171 Ancient Sedimentary Organic Matter: New Evidence from Australia and South Africa.  
1172 *Geology* 2, 591-595.
- 1173 Mehmood, M., Yaseen, M., Khan, E. U., Khan, M. J. 2018. Dolomite and Dolomitization Model  
1174 – A Short Review. *Int J Hydro.* 2(5), 549-553.
- 1175 Miller, B. L. 1941. *LeHigh County Pennsylvania: Geology and Geography, Pennsylvania*  
1176 *Geological Survey Bulletin, 4<sup>th</sup> Series C 39.* Harrisburg, PA.

- 1177 Monteverde, D.H. 1992. Bedrock geologic map of Sussex County, New Jersey, portions of the  
1178 Culvers Gap and Lake Maskenozha quadrangles, New Jersey Geological Survey Geologic  
1179 Map, 92-1.
- 1180 Moore, C. H. 1989. Carbonate Diagenesis and Porosity, in *Developments in Sedimentology*, 46,  
1181 Amsterdam, Elsevier, 46-338.
- 1182 Morrow, D.W. 1982. Diagenesis II. Dolomite—Part II: Dolomitization Models and Ancient  
1183 Dolostones. *Geoscience Canada* 9, 95-107.
- 1184 Mueller, M., Igbokwe, O. A., Walter, B., Pederson, C. L., Riechelmann, S., Richter, D. K., Albert,  
1185 R., Gerdes, A., Buhl, D., Neuser, R. D., Bertotti, G., Immenhauser, A. 2019. Testing the  
1186 preservation potential of early diagenetic dolomites as geochemical archives. *Sedimentology*,  
1187 67(2), 849-881.
- 1188 Mustard, J. F., Adler, M., Allwood, A., Bass, D. S., Beaty, D. W., Bell III, J. F., Brinckerhoff, W.  
1189 B., Carr, M., Des Marais, D. J., Drake, B., Edgett, K. S., Eigenbrode, J., Elkins-Tanton, L. T.,  
1190 Grant, J. A., Milkovich, S. M., Ming, D., Moore, C., Murchie, S., Onstott, T. C., Ruff, S. W.,  
1191 Sephton, M. A., Steele, A., Treiman, A. 2013. Report of the Mars 2020 Science Definition  
1192 Team, 154 pp., posted July 2013, by the Mars Exploration Program Analysis Group (MEPAG)  
1193 at [http://mepag.jpl.nasa.gov/reports/MEP/Mars\\_2020\\_SDT\\_Report\\_Final.pdf](http://mepag.jpl.nasa.gov/reports/MEP/Mars_2020_SDT_Report_Final.pdf).
- 1194 Nordeng, S. H., Sibley, D. F. 1994. Dolomite stoichiometry and Ostwald's Step Rule. *Geochim.*  
1195 *Cosmochim. Acta* 58, 191-196.
- 1196 Oehlert, A. M., Swart, P. K. 2014. Interpreting carbonate and organic carbon isotope covariance  
1197 in the sedimentary record. *Nat. Commun.* 5, 1–7.
- 1198 Pasteris, J. D., Wopenka, B. 1991. Raman spectra of graphite as indicators of degree of  
1199 metamorphism. *Can. Mineral.* 20, 1-9.

- 1200 Pasteris, J. D., Wopenka, B. 2003. Necessary, but not sufficient: Raman identification of  
1201 disordered carbon as a signature of ancient life. *Astrobiology* 3(4), 727-38.
- 1202 Plummer, P. S., Gostin, V. A. 1981. Shrinkage cracks: desiccation or syneresis. *J. Sediment.*  
1203 *Petrol.* 51, 147-1156.
- 1204 Pratt, B. R., James, N. P., Cowan, C. A. 1992. Peritidal carbonates, in: Walker, R. G., James, N.  
1205 P. (Eds.), *Facies Models – Response to Sea Level Change*. Geological Association of Canada,  
1206 303-322.
- 1207 Rao, V. P., Kessarkar, P. M., Krumbein, W. E., Krajewski, K. P., Schneider, R. J. 2003. Microbial  
1208 dolomite crusts from the carbonate platform off western India. *Sedimentology* 50, 819-830.
- 1209 Richter, D. K., Götze, T., Götze, J., Neuser, R. D. 2003. Progress in application of  
1210 cathodoluminescence (CL) in sedimentary petrology. *Mineral. Petrol.* 79(3-4), 127-166.
- 1211 Sanz-Montero, M. E., Rodríguez-Aranda, J. P., García del Cura, M. A. 2008. Dolomite-silica  
1212 stromatolites in Miocene lacustrine deposits from the Duero Basin, Spain: the role of  
1213 organotemplates in the precipitation of dolomite. *Sedimentology* 55, 729-750.
- 1214 Schidlowski, M. 1988. A 3,800-million-year isotopic record of life from carbon in sedimentary  
1215 rocks. *Nature* 333, 313-318.
- 1216 Scholle, P. A., Ulmer-Scholle, D. S. 2003. *A Color Guide to the Petrography of Carbonate Rocks:*  
1217 *Grains, Textures, Porosity, Diagenesis*. AAPG Memoir 77.
- 1218 Schopf, J. W. 1999. *Cradle of Life: The Discovery of Earth's Earliest Fossils*. Princeton University  
1219 Press, Princeton, NJ.
- 1220 Schopf, J. W., Kudryavtsev, A. B. 2012. Biogenicity of Earth's earliest fossils: A resolution of the  
1221 controversy. *Godwana Research* 22(3-4), 761-771.
- 1222 Sharp, Z. 2007. *Principles of Stable Isotope Geochemistry*. Pearson Prentice Hall.

- 1223 Sibley D. 1978. Dolomite textures, in: Middleton, G. V., Church, M. J., Coniglio, M., Hardie,  
1224 L. A., Longstaffe, F. J. (Eds.), *Encyclopedia of Sediments and Sedimentary Rocks*.  
1225 *Encyclopedia of Earth Sciences Series*. Springer, Dordrecht.
- 1226 Sibley, D. F., Gregg, J. M. 1987. Classification of Dolomite Rock Textures. *J. Sed. Petrol.* 57(6),  
1227 967-975.
- 1228 Sibley D. F. 1991. Secular changes in the amount and texture of dolomite. *Geology* 19(2), 151-  
1229 154.
- 1230 Sijing, H., Keke, H., Jie, Lu, Yefang, L. 2014. The relationship between dolomite textures and  
1231 their formation temperature: a case study from the Permian-Triassic of the Sichuan Basin  
1232 and the Lower Paleozoic of the Tarim Basin. *Pet. Sci.* 11, 39-51.
- 1233 Stead, R. J., Kodama, K. P. 1984. Paleomagnetism of the Cambrian Rocks of the Great Valley if  
1234 East Central Pennsylvania: Fold Test Constraints on the Age of Magnetization, Plate  
1235 reconstruction, in: *Paleozoic paleomagnetism: Interim report of the Working Group 2 on*  
1236 *Phanerozoic Plate Motions and Orogenesis*. Washington, D. C.: American Geophysical Union.
- 1237 Strauss, H., Beukes, N. J. 1996. Carbon and sulfur isotopic compositions of organic carbon and  
1238 pyrite sediments from the Transvaal Supergroup, South Africa. *Precamb. Res.* 79, 57-71.
- 1239 Sugitani, K., Grey, K., Allwood, A., Nagaoka, T., Mimura, K., Minami, M., Marshall, C. P., Van  
1240 Kranendonk, M. J., Walter, M. R. 2007. Diverse microstructures from Archaean chert from the  
1241 Mount Goldsworthy–Mount Grant area, Pilbara Craton, Western Australia: Microfossils,  
1242 dubiofossils, or pseudofossils? *Precamb. Res.* 158(3-4), 228-262.
- 1243 Swart, P. K. 2015. The geochemistry of carbonate diagenesis: The past, present and future.  
1244 *Sedimentology* 62, 1233-1304.

- 1245 Tilley, C. 1924. The Facies Classification of Metamorphic Rocks. *Geological Magazine* 61(4),  
1246 167-170.
- 1247 Tucker, M., Wright, V. P. 1990. *Carbonate Sedimentology*. Black-Well Scientific Publications,  
1248 Oxford.
- 1249 Van Kranendonk, M. J., Webb, G. E., Kamber, B. S. 2003. Geological and trace element evidence  
1250 for a marine sedimentary environment of deposition and biogenicity of 3.45 Ga stromatolitic  
1251 carbonates in the Pilbara Craton, and support for a reducing Archaean ocean. *Geobiology* 1(2),  
1252 91-108.
- 1253 Voelz, J. L., Johnson, N. W., Chun, C. L., Arnold, W. A., Penn, R. L. 2019. Quantitative  
1254 Dissolution of Environmentally Accessible Iron Residing in Iron-Rich Minerals: A Review.  
1255 *ACS Earth Space Chem.* 3, 1371-1392.
- 1256 Warren, J. 2000. Dolomite: occurrence, evolution, and economically important associations.  
1257 *Earth-Sci. Rev.* 52(1-3), 1-81.
- 1258 Weller, S. 1903. The Paleozoic faunas: New Jersey Geological Survey Report on Paleontology, 3.
- 1259 Wilson J. L. 1975. *Carbonate Facies in Geologic History*, Springer-Verlag, New York.
- 1260 Witte, R. W., Monteverde, D. H. (2012) *Geologic History of New Jersey's Valley and Ridge*  
1261 *Physiographic Province*, New Jersey Geological and Water Survey Information Circular,  
1262 Trenton, NJ.
- 1263 Wopenka, B., Pasteris, J. D. 1993. Structural characterization of kerogens to granulite-facies  
1264 graphite: Applicability of Raman microprobe spectroscopy. *Amer. Miner.* 78, 533-557.
- 1265 Zhang, F., Xu, H., Shelobolina, E. S., Konishi, H., Converse, B., Shen, Z., Roden, E. E. 2015.  
1266 The catalytic effect of bound extracellular polymeric substances excreted by anaerobic

- 1267 microorganisms on Ca-Mg carbonate precipitation: Implications for the “dolomite problem”.  
1268 Amer. Miner. 100(2-3), 483–494.
- 1269 Zhang, J., Hu, W., Qian, Y., Wang, X., Cao, J., Zhu, J., Li, Q., Xie, X. 2009. Formation of saddle  
1270 dolomites in Upper Cambrian carbonates, western Tarim Basin (northwest China):  
1271 Implications for fault-related fluid flow. Mar. Petrol. Geol. 26, 1428-1440.